1-28-2015

Defect investigations in InAs/GaSb type-II strained layer superlattice

Brianna Klein

Brianna Klein
Candidate

Electrical and Computer Engineering
Department

This dissertation is approved, and it is acceptable in quality and form for publication:

Approved by the Dissertation Committee:

Dr. Sanjay Krishna , Chairperson

Dr. Sumith Bandara

Dr. Kevin Malloy

Dr. Ganesh Balakrishnan

DEFECT INVESTIGATIONS IN InAs/GaSb TYPE-II STRAINED LAYER SUPERLATTICE

BY

BRIANNA KLEIN

B.S. ELECTRICAL ENGINEERING
NEW MEXICO INSTITUTE OF MINING AND TECHNOLOGY, 2008

M.S. ELECTRICAL ENGINEERING
NEW MEXICO INSTITUTE OF MINING AND TECHNOLOGY, 2009

DISSERTATION

Submitted in Partial Fulfillment of the
Requirements for the Degree of

Doctor of Philosophy

Engineering

The University of New Mexico
Albuquerque, New Mexico

December 2014

ACKNOWLEDGEMENTS

So many people have helped make this dissertation possible. First, I could have not done this without the support and encouragement of my advisor, Dr. Sanjay Krishna. Even when he became in charge of CHTM, and had no time at all, he still was able to answer all of my questions and keep me going in the right direction. My dissertation committee, Dr. Sumith Bandara, Dr. Kevin Malloy, and Dr. Ganesh Balakrishnan have been there to ask the right questions and help my work progress. It has been great to have their expertise available for this project.

My group, my friends, and my family have been here with me every step of the way. It has been an honor to work with all of my group members and lab buddies, past and present. The students before me, Nutan, Ajit, Stephen M, Stephen C, Ha Sul, Arezou, Rajeev, Maya, David, Eric, and Pankaj, I have looked up to all of you and learned what it means to be a hard-working graduate student. The students still here with me, Lilian, Happy, Emma, John, Ted, Clark, Zahra, Ali, Rhett, Noel, Leisha, Saadat, and Mitch, you all have asked me so many questions, many that I couldn't have come up with on my own, that help keep me on my toes. A special thank you to everyone in the WHAAAAAAT club! And there are all the people who I have gotten to work with, teach, and be taught by, Nathan, Shaleena, Zoe, Orlando, Mikhail, Sean, Tom, Sen, and Jun Oh. I give a special thanks to Elena, who taught me so much about writing papers, working with people, and above all, being persistent.

I would also like to thank the many people that keep CHTM going: Joel, Dan, Rick, Douglas, Steve, Beth, Andrew, Joe M, Mike, Lee, Ron, Josh, Pat, Joe S, Wesley, Tamara, Jessica, Pam, Karen, Linda, and Stefi. Janell, you have helped me out so much! It was great to have Chris around too, with his delightful cynicism.

My brother Mike, my Mom, and my Dad have been cheering me on the entire time and supporting me when I needed help. The same is true for the Sammons,

Linda, Don, Kevin, Theresa, and Chris N.! Thank you all for being here for me!

My after-work friends have also helped me by helping me relax. Thanks to Zeb, Eric, Cynthia, Steve, Chris W., and Isabella!

Last of all, I could not have done this without my awesome boyfriend Jason, who helped me out when I was sick, rescued me when I had bike troubles, and made sure that I didn't forget to eat.

DEFECT INVESTIGATIONS IN InAs/GaSb TYPE-II STRAINED LAYER SUPERLATTICE

by

Brianna Klein

B.S. Electrical Engineering
New Mexico Institute of Mining and Technology, 2008

M.S. Electrical Engineering
New Mexico Institute of Mining and Technology, 2009

PhD, Engineering
University of New Mexico, 2014

ABSTRACT

InAs/GaSb type-II strained layer superlattices are a material used for infrared detection. By adjusting the thickness of the InAs and GaSb layers, the material bandgap can be tuned to absorb photons from 3-30 μm. Compared to competing materials such as HgCdTe and InSb, InAs/GaSb superlattices are more mechanically robust, have reduced tunneling currents, and can use strain to suppress Auger recombination. In spite of these advantages, this material still faces several challenges, including low minority carrier lifetime, resulting from trap levels that cause Schockley-Read-Hall recombination. These low lifetimes lead to reduced signal-to-noise ratio and higher dark current. Therefore, increasing the lifetime is important for improving this material's performance. However, to increase the carrier lifetimes, the origin of the traps must first be understood.

In this work, several key suspect causes of the "killer" defect were evaluated.

A commonly explored suspect in literature, the interfaces, was studied using time-resolved photoluminescence for three different samples. This characterization method was also used to determine if the doping atom and its layer placement significantly impacted the minority carrier lifetime. There is a substantial amount of evidence that the presence of gallium, or the GaSb layer itself harbors the defect. Thus, the rest of the study focused on aspects of GaSb. Layer intermixing of the In and As atoms into the GaSb layer was studied by intentionally incorporating In and As in bulk GaSb and using photocapacitance characterization to observe any possible defect level formation. In addition, trap level formation for different GaSb growth temperatures was also explored with this characterization technique. Finally, in an attempt to reduce trap densities, GaSb was grown with an increased level of Sb monomers rather than dimers. This material was characterized using dark current density measurements and photoluminescence.

Contents

List of Figures

List of Tables

Chapter 1

Introduction

InAs/GaSb type-II strained layer superlattices (T2SL) have the potential to be a very useful infrared detector material. Their main competitor is the tried-and-true HgCdTe which is a mature technology that originated in the 1950's. Even though T2SL system (proposed in the late 1970's) has better compositional uniformity, larger substrates, is more mechanically robust, and suppressed Auger recombination, all of which are major problems in the HgCdTe system, it has a fatal flaw that continues to hold it back. The minority carriers (electrons or holes) have such short lifetimes ($\sim$ 30 ns for LWIR, $\sim$ 100 ns for MWIR) that many of them die before they can reach the contacts and produce a signal. This reduces the signal-to-noise ratio and leads to larger dark currents; this problem alone renders T2SL a less desirable material than HgCdTe. In order to gain a competitive edge, the minority carrier lifetimes must be increased by at least an order of magnitude. The way to end this is to get rid of whatever is killing the carriers. However, while we have clues, much about the killer remains unknown.

Two decades [1] have passed since the Shockley-Read-Hall recombination (SRH) process was identified as the killer. This type of recombination is caused by defects, typically with energies in the middle of the bandgap, that act as places for an electron

and hole (lack of electron) to annihilate each other. These defects could be caused by a number of different things such as contaminants, crystallographic interfaces, intermixing of the T2SL layers, and growth temperature, to name a few. So, although it is well-known that defects are responsible for the deaths of the charge carriers, an exact cause has yet to be identified.

This thesis documents the search for this illusive defect to make the T2SL a safer place for the electron and hole. The scope of this work is limited to mid-wave (3-5 μm) infrared material. First, what we already know about T2SL and defect is described in Chapter 2. This information leads us to some suspects (see figure 1), including T2SL interfaces and the constituent T2SL materials themselves. The charge carrier "murder investigation" is then described in Chapters 4 and 5, using such characterization methods as photocapacitance, time-resolved photoluminescence, and dark current levels to try to catch the killer red-handed. Finally, we reach the harrowing conclusion in Chapter 6, which also outlines future work.

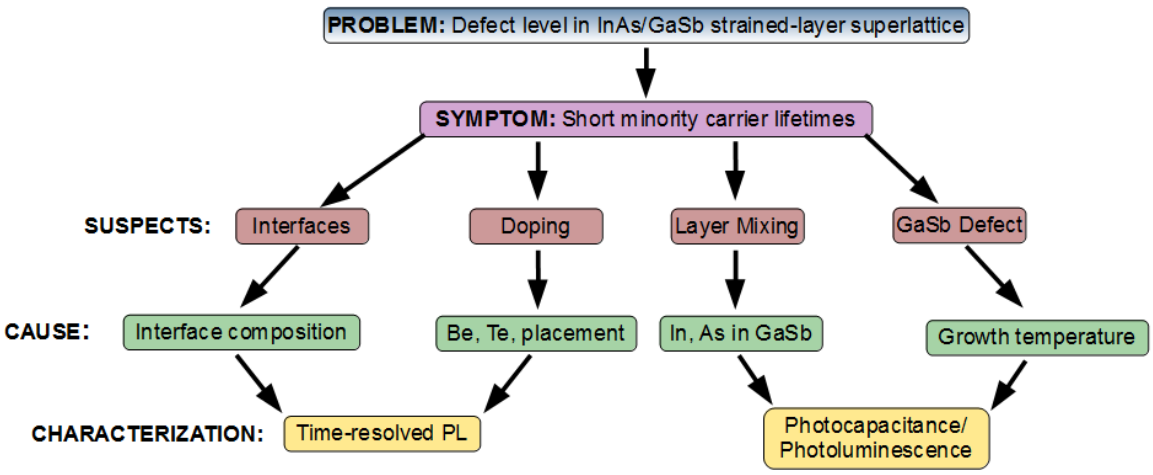

Figure 1.1: Map showing scope of work. The problem being addressed is a defect in T2SL, which causes short minority carrier lifetimes in T2SL, while interfaces and constituent materials are investigated as possible culprits, subsets of the culprits are below, and finally methods used to characterized them are below that.

Contributions of dissertation:

1. Uses photocapacitance measurements to study traps in GaSb for improving the lifetime of the charge carriers in InAs/GaSb superlattice:
    - Layer intermixing (effect of GaSb mixed with In and As)
    - Growth temperature (effect of growing GaSb at its optimal temperature compared to growing it at the T2SL growth temperature)
    - Effect growing GaSb with various Sb cracking zone temperatures (which produces different ratios of Sb monomers and dimers)
2. Compares the effect on carrier lifetime of different interfaces formed by using the following between InAs and GaSb layers:
    - growth interrupts
    - InSb strain compensation layers
    - Sb soaks
3. Compares effect on carrier lifetime for different doping atoms and their placement within the superlattice layers
    - Beryllium
    - Tellurium
    - InAs layer doped
    - GaSb layer doped
    - All layers doped

Publications

- B. Klein, E. Plis, M. N. Kutty, N. Gautam, a Albrecht, S. Myers, and S. Krishna, *"Varshni parameters for InAs/GaSb strained layer superlattice infrared photodetectors,"* J. Phys. D. Appl. Phys., vol. 44, no. 7, p. 075102, Feb. 2011.

- B. Klein, J. Montoya, N. Gautam, and S. Krishna, *"Selective InAs/GaSb strained layer superlattice etch stop layers for GaSb substrate removal,"* Appl. Phys. A Mater. Sci. Process., vol. 111, no. 2, pp. 671674, 2013.

- B. Klein, N. Gautam, E. Plis, T. Schuler-sandy, T. J. Rotter, S. Krishna, B. Connelly, G. D. Metcalfe, P. Shen, and M. Wraback, *"Carrier lifetime studies in midwave infrared type-II InAs / GaSb strained layer superlattice"* J. Vac. Sci. Technol. B, vol. 32, no. 2, p. 02C101, 2014.

- E. Plis, B. Klein, S. Myers, N. Gautam, and S. Krishna, *"(111) InAs/GaSb type-II strained layer superlattice material for high operating temperature detection,"* Phys. Status Solidi, vol. 10, no. 5, pp. 748751, May 2013.

- E. Plis, B. Klein, S. Myers, N. Gautam, T. J. Rotter, R. L. Dawson, S. Krishna, S. J. Lee, and Y. H. Kim, *"Type-II InAs/GaSb strained layer superlattices grown on GaSb (111)B substrate,"* J. Vac. Sci. Technol. B, vol. 31, no. 3, p. 03C123, 2013.

- E. Plis, B. Klein, S. Myers, N. Gautam, E. P. Smith, and S. Krishna, *"High Operating Temperature Midwave Infrared InAs / GaSb Superlattice Photodetectors,"* IEEE Electron Device Lett., vol. 34, no. 3, pp. 426428, 2013.

- G. A. Umana-Membreno, B. Klein, H. Kala, J. Antoszewski, N. Gautam, M. N. Kutty, E. Plis, S. Krishna, and L. Faraone, *"Vertical minority carrier electron*

transport in p-type InAs/GaSb type-II superlattices," Appl. Phys. Lett., vol. 101, no. 25, p. 253515, 2012.

- G. A. Umana-Membreno, B. Klein, E. P. G. Smith, J. Antoszewski, E. Plis, S. M. Johnson, S. Krishna, D. R. Rhiger, and L. Faraone, *"Electron Transport in InAsSb-Based nBn Photodetector Structures,"* IEEE Trans. Electron Devices, vol. 60, no. 1, pp. 510512, Jan. 2013.

- N. Gautam, H. S. Kim, S. Myers, E. Plis, M. N. Kutty, M. Naydenkov, B. Klein, L. R. Dawson, and S. Krishna, *"Heterojunction bandgap engineered photodetector based on type-II InAs/GaSb superlattice for single color and bicolor infrared detection,"* Infrared Phys. Technol., vol. 54, no. 3, pp. 273277, May 2011.

- N. Gautam, S. Myers, A. V. Barve, B. Klein, E. P. Smith, D. Rhiger, E. Plis, M. N. Kutty, N. Henry, T. Schuler-Sandy, and S. Krishna, *"Band engineered HOT midwave infrared detectors based on type-II InAs/GaSb strained layer superlattices,* Infrared Phys. Technol., vol. 59, pp. 7277, Jul. 2013.

- N. Gautam, S. Myers, A. V Barve, B. Klein, E. P. Smith, D. R. Rhiger, H. S. Kim, Z.-B. Tian, and S. Krishna, *"Barrier Engineered Infrared Photodetectors Based on Type-II InAs / GaSb Strained Layer Superlattices,"* IEEE J. Quantum Electron., vol. 49, no. 2, pp. 211217, 2013.

- N. Gautam, S. Myers, A. V. Barve, B. Klein, E. P. Smith, D. R. Rhiger, L. R. Dawson, and S. Krishna, High operating temperature interband cascade midwave infrared detector based on type-II InAs/GaSb strained layer superlattice, Appl. Phys. Lett., vol. 101, no. 2, p. 021106, 2012.

- A. V Barve, S. Sengupta, J. O. Kim, J. Montoya, B. Klein, M. A. Shirazi, M. Zamiri, Y. D. Sharma, S. Adhikary, S. E. Godoy, W. Jang, G. R. C. Fiorante,

S. Chakrabarti, and S. Krishna, *"Barrier Selection Rules for Quantum Dots-in-a-Well Infrared Photodetector,"* IEEE J. Quantum Electron., vol. 48, no. 10, pp. 12431251, 2012.

- T. Schuler-Sandy, S. Myers, B. Klein, N. Gautam, P. Ahirwar, Z.-B. Tian, T. Rotter, G. Balakrishnan, E. Plis, and S. Krishna, *"Gallium free type II InAs/InAsxSb1-x superlattice photodetectors,"* Appl. Phys. Lett., vol. 101, no. 7, p. 071111, Aug. 2012.

- S. A. Colgate, H. Beckley, J. Si, J. Martinic, D. Westpfahl, J. Slutz, C. Westrom, B. Klein, P. Schendel, C. Scharle, T. McKinney, R. Ginanni, I. Bentley, T. Mickey, R. Ferrel, H. Li, V. Pariev, and J. Finn, *"High Magnetic Shear Gain in a Liquid Sodium Stable Couette Flow Experiment: A Prelude to an $\alpha - \Omega$ Dynamo,"* Phys. Rev. Lett., vol. 106, no. 17, p. 175003, Apr. 2011.

Conference Proceedings

- B. Klein, N. Gautam, S. Myers, and S. Krishna, *"Temperature-dependent absorption derivative on InAs/GaSb Type II superlattices,"* Proc. SPIE, vol. 8353, 2012.

- B. Klein, *"Temperature-dependent behavior of InAsSb and InAs/GaSb strained layer superlattice infared photodetectors,"* in 23rd Annual Meeting of the IEEE Photonics Society, 2010, 2010, no. 2008, pp. 639640.

- S. Myers, E. Plis, C. Morath, V. Cowan, N. Gautam, B. Klein, M. N. Kutty, M. Naydenkov, T. Schuler-Sandy, and S. Krishna, *"Comparison of superlattice based dual color nBn and pBp infrared detectors,"* Proc. SPIE, vol. 8155, p. 815507, Sep. 2011.

- E. Plis, B. Klein, N. Gautam, S. Myers, M. N. Kutty, M. Naydenkov, and S. Krishna, *"Performance optimization of long-wave infrared detectors based on InAs/GaSb strained layer superlattices,"* Proc. SPIE, vol. 8012, p. 80120V, May 2011.

- G. A. Umana-Membreno, B. Klein, H. Kala, J. Antoszewski, N. Gautam, M. N. Kutty, E. Plis, S. Krishna, and L. Faraone, *"Vertical transport in InAs / GaSb type-II superlattices,"* in 2012 Conference on Optoelectronic and Microelectronic Materials & Devices (COMMAD), 2012, pp. 56.

- G. A. Umana-Membreno, H. Kala, B. Klein, J. Antoszewski, N. Gautam, M. N. Kutty, E. Plis, S. Krishna, and L. Faraone, *"Electronic transport in InAs/GaSb type-II superlattices for long wavelength infrared focal plane array applications,"* in Proc. SPIE 8353, Infrared Technology and Applications XXXVIII, 2012, p. 83530Y.

- A. Khoshakhlagh, S. Myers, E. Plis, M. N. Kutty, B. Klein, N. Gautam, H. Kim, E. P. G. Smith, D. Rhiger, S. M. Johnson, and S. Krishna, *"Mid-wavelength InAsSb detectors based on nBn design,"* in Proc. SPIE 7660, Infrared Technology and Applications XXXVI, 2010, p. 76602Z.

- S. A. Myers, A. Khoshakhlagh, J. Mailfert, P. Wanninkhof, E. Plis, M. N. Kutty, H. S. Kim, N. Gautam, B. Klein, E. P. G. Smith, and S. Krishna, *"Performance of InAsSb-based infrared detectors with nBn design,"* in Proc. SPIE 7808, Infrared Remote Sensing and Instrumentation XVIII, 2010, p. 780805.

- N. Gautam, A. V Barve, S. Myers, B. Klein, E. Plis, M. Naydenkov, N. Maya, T. Schuler-Sandy, and S. Krishna, *"Polarization Selective Interband Transitions in Type-II InAs / GaSb Superlattices,"* in 2011 IEEE Photonics Conference (PHO), 2011, vol. 14, pp. 3334.

- E. A. Plis, N. Gautam, M. N. Kutty, S. Myers, B. Klein, T. Schuler-Sandy, M. Naydenkov, and S. Krishna, *"Performance of long-wave infrared InAs/GaSb strained layer superlattice detectors for the space applications,"* in Proc. SPIE 8164, Nanophotonics and Macrophotonics for Space Environments V, 2011, vol. 8164, p. 81640S.

- S. Myers, E. Plis, C. Morath, V. Cowan, N. Gautam, B. Klein, M. N. Kutty, M. Naydenkov, T. Schuler-Sandy, and S. Krishna, *"Comparison of superlattice based dual color nBn and pBp infrared detectors,"* in Proc. SPIE 8155, Infrared Sensors, Devices, and Applications; and Single Photon Imaging II, 2011, vol. 8155, p. 815507.

- Z.-B. Tian, T. Schuler-Sandy, S. E. Godoy, H. S. Kim, J. Montoya, S. Myers, B. Klein, E. Plis, and S. Krishna, *"Quantum-engineered mid-infrared type-II InAs/GaSb superlattice photodetectors for high temperature operations,"* in Proc. SPIE 8704, Infrared Technology and Applications XXXIX, 2013, p. 87041T.

- E. Plis, N. Gautam, B. Klein, S. Myers, T. Schuler-Sandy, M. N. Kutty, Z.-B. Tian, and S. Krishna, *"Performance of single-and dual-color detectors using InAs/GaSb strained layer superlattices,"* in 2012 Lester Eastman Conference on High Performance Devices (LEC), 2012, pp. 14.

Chapter 2

Basics of InAs/GaSb Type-II Strained Layer Superlattices

This chapter provides the foundation to understand InAs/GaSb type-II strained layer superlattices. Before diving into the details of IR detectors, a description of the electromagnetic spectrum is provided, detailing the different parts of the infrared range. This is followed by applications of infrared detectors, a discussion of the different sensing techniques, and types of infrared sensors. Finally, InAs/GaSb strained layer superlattices are discussed, including a brief history, its best performance metrics, and its advantages and challenges.

2.1 Infrared spectrum, detectors, and applications

Since the discovery of the invisible realms of the electromagnetic spectrum [2] people have endeavored to understand and harness its usefulness. Between wavelengths of 10 nm and 1 mm lies the realm useful for optics and optoelectronic devices. This consists of the ultra-violet (10-400 nm), visible (400-700 nm), and infrared (IR) (700 nm - 1 mm) regions. The infrared can be further segmented by atmospheric transmission windows, sections of the IR spectrum which are transmitted through earth's

atmosphere. The near-IR (0.75 μm - 1.4 μm), short-wave IR (1.4-3 μm), mid-wave IR (MWIR) (3-5 μm), long-wave IR (LWIR) (8-12 μm), and very-long wave IR (30μm - 1mm). For example, the near- and short-wave IR is often used for fiber-optic communication, while MWIR and LWIR are of interest for infrared cameras. Humans beings also emit IR, with a peak intensity corresponding to approximately 9.2 μm. Thus, the ability to sense photons in the LWIR allows us to observe people in ways that would otherwise indiscernible by cameras operating in the visible.

There are numerous applications for IR detectors, including night vision, navigation, security and surveillance, atmospheric monitoring, and astronomy [3]. IR detectors are used in multi-spectral imaging which allows monitoring of vegetation health or amount of water, from satellite views of the earth. The atmospheric composition can be monitored by IR sensors, search and rescue utilizes IR cameras to find missing people, and defects in fruit can be observed long before the fruit shows signs of decay in the visible wavelengths.

Because IR detectors have so many uses, many different methods for sensing IR have been developed. Thermal IR detectors, such as thermometers, Golay cells, pyroelectric detectors, and Bolometers, operate by absorbing photons which heats up the detector and changes some measurable physical property of the detector [2]. Photon detectors work by incident photon interaction with electrons [2] and are made of semiconductors of numerous structures (bulk semiconductor, quantum well, quantum dot, quantum dot-in-well, and superlattices) and materials (InSb, HgCdTe, Si:X) [4]. Each of these IR detectors has its own drawbacks as well as advantages. Thermal detectors are much slower and less responsive than photon detectors, as it takes time for them to heat. Photon detectors, especially for MWIR and LWIR, often have to by cryogenically cooled in order to operate. Rivalries between photon detectors also exist. HgCdTe and InSb are mature, dominant detector technologies for MWIR (InSb, HgCdTe) and LWIR (HgCdTe) applications, but are followed closely in device per-

formance by younger technologies utilizing quantum confinement and heterostructure engineering. One such material, InAs/GaSb strained-layer superlattice (SLS) has the potential to beat the dominant technologies.

Many of the optoelectronic devices we know today could not have been made without the realization of heterostructures [5, 6]. At their simplest, heterostructures are semiconductors made of two different materials joined together at an abrupt junction; this configuration consists two materials of dissimilar bandgap [7, 8]. A classic example is AlGaAs and GaAs, which forms the basis for one type of semiconductor laser. This concept of a heterostructure seems rather simple, yet was revolutionary at its inception. An abrupt transition from one semiconductor material to another offered superior control of junction location, which was unattainable with dopant atoms. Further, the refractive index was also abruptly changed with the heterojunction; not only could spatially abrupt junctions be formed, but also could be doubly used as waveguides [8]. The concept of heterostructures paved the way for many new types of semiconductor materials, such as quantum wells, quantum wires, quantum dots, and superlattices.

2.2 InAs/GaSb Type-II Strained Layer Superlattices

InAs/GaSb type-II strained layer superlattices are made by alternating thin (6-30 monolayers, or 18-100 Å) InAs and GaSb layers, as shown in figure 2.1. A set of one InAs and GaSb layer comprises a single period of the superlattice; the thickness of each layer of InAs and GaSb together dictate the bandgap formed by the superlattce. The story of the superlattice began in 1970, when it was first conceptualized by Nobel laureate Leo Esaki and his colleague Ray Tsu [9]. They predicted that if alternating layers of material, either through doping or by heterojunction, had thin enough

periods, a new set of allowed and forbidden energy levels would form. It took the greater part of a decade, however, for the concept of a broken-gap superlattice to be introduced [10]. A broken gap superlattice was special compared to previous designs, consisting of two materials with band alignments so different that the valence band of one material is above the conduction band of the other. This unusual band alignment caused spatial de-localization of the charge carriers; the GaSb confines the holes and InAs confines the electrons, leading to independent tunability of the conduction and valence band edges [11]. Finally, in 1987, Smith and Mailhiot proposed that InAs/GaSb type-II strained-layer superlattice (T2SL) was an advantageous material for infrared detection because of its bandgap tunability, and small diode tunneling currents, good mobilities and diffusion lengths [12].

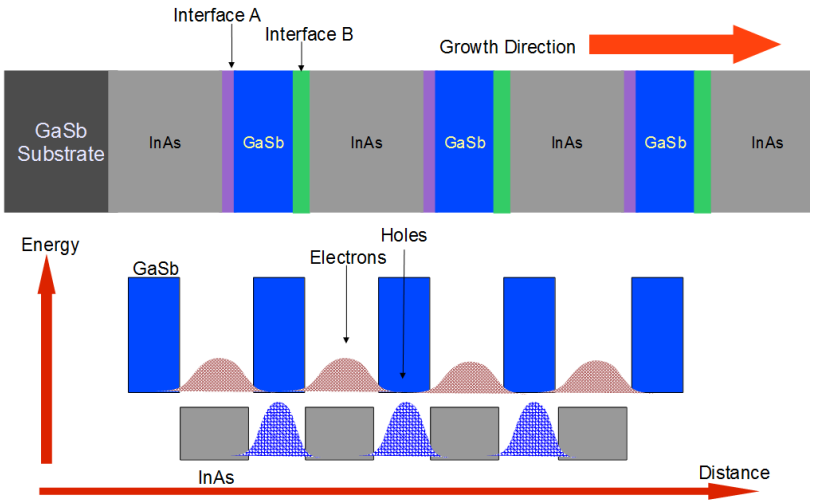

Figure 2.1: InAs/GaSb type-II strained layer superlattice structure and electron-hole interaction.

Today, T2SL is usually grown by molecular beam epitaxy (MBE), though a few attempts have also been made through metalorganic chemical vapor deposition (MOCVD) [13, 14]. The mature techniques of III-V processing have enabled the fabrication of focal plane arrays (FPA), ranging in size from 288 x 384 [15] to 1K x 1K pixels [16]. Rule 07 [17, 18], a benchmark that defines the state-of-the art dark

currents of HgCdTe, has become the operating goal for T2SL to outperform.

T2SL has shown to have several advantages. It is part of the "6.1 Å family" [19] consisting of InAs, GaSb, AlSb, and InSb, which can be combined to produce a number of heterostructure designs, including the nBn [20], CBIRD [21], M-Structure [22], pBiBn [23], and interband cascade [24], which would be difficult to make with other IR detector materials. InAs and GaSb also have much stronger chemical bonds [2] and a higher degree of mechanical robustness [11] than their more common counterparts, such as HgCdTe and InSb, making them easier to grow and manufacture. Because of their higher effective mass, the T2SL also suppresses band-to-band tunneling, which allows for their absorber region to be doped at least an order of magnitude higher than HgCdTe, thus improving their signal-to-noise ratio [25]. Although InAs and GaSb have similar lattice constants, T2SL still have a considerable amount of strain. This strain, along with quantum confinement, causes the light- and heavy-hole valence bands to separate energetically; if the separation exceeds the bandgap, Auger recombination becomes suppressed [26, 1]. With all of these advantages, T2SL is the only IR detector material that is theoretically capable of out-performing HgCdTe [27].

Despite the many advantages of T2SL, this material has yet to live up to its theoretical performance predictions. Because of its inhomogeneous dispersion relation, the mobility of its charge carriers in the direction of intended current flow (vertical mobility) is low compared to the mobility in other directions (lateral mobility) [28]. Furthermore, because T2SL has no common cation or anion between its two constituents, a reliable passivation method to alleviate surface leakage current [29] has yet to be developed. Additionally, although Auger recombination can be suppressed [1], T2SL is wrought with Shockley-Read-Hall recombination [30], reducing its minority carrier lifetime by 2-3 orders of magnitude less than HgCdTe. Realistically, in order for T2SL to be a competitive IR detector material, solutions to these problems

must be found.

2.3 Recombination mechanisms in semiconductors

Photon detectors operate by electrons interacting with incident photons. The detector material absorbs photons with enough energy to form electron-hole pairs, using the energy imparted from the photon to promote an electron to the conduction band. If an electric field is also present, either by a junction or applied reverse bias, the electron and hole pairs can be separated spatially and drawn to metal contacts of the device. Thus, a photocurrent is formed and can be measured. The more charge carriers that reach the contacts, the stronger the photocurrent signal and the higher the signal-to-noise ratio (SNR). Unfortunately, not all of the charge carriers live long enough to reach the contacts and contribute to the signal; there are several ways that the an electron in the conduction band can recombine with a hole that satisfy energy and momentum conservation, including radiative, Shockley-Read-Hall, Auger, and surface recombination. Refer to figure 2.2 as each of these processes is described.

When an electron in the conduction band returns to directly a hole in the valence band, emitting a photon of energy approximately equal to the bandgap, **radiative (or bimolecular) recombination** has occurred. While all semiconductor materials have radiative recombination, it happens much more readily in direct rather than indirect bandgap materials [32]. Band-to-band photon emission rate is [32]

$$R_{rad} = Bnp \tag{2.1}$$

where n and p are the electron and hole densities, and B is the radiative recombination coefficient (cm^3/s). This rate is dependent on the material itself, specifically the electron and hole effective masses, m_n and m_p, as well as the bandgap (E_g) and the

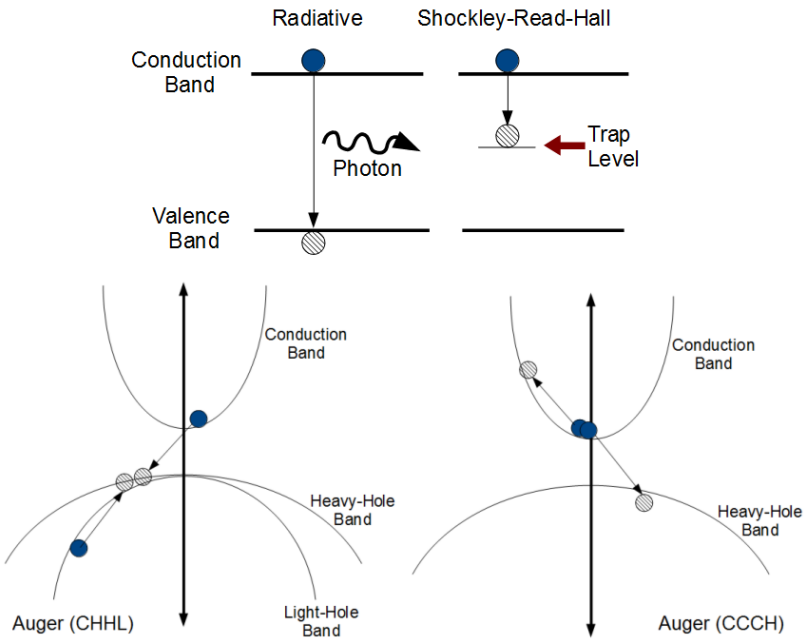

Figure 2.2: Recombination mechanisms in semiconductors. Radiative and Shockley-Read-Hall are shown on the top, and two possible Auger recombination processes [31] are on the bottom.

material temperature (T) [32]:

$$B \propto \left(\frac{1}{m_p + m_n}\right)^{3/2} \left(1 + \frac{1}{m_p} + \frac{1}{m_n}\right) \left(\frac{300}{T}\right)^{3/2} E_g^2 \tag{2.2}$$

The effective mass in this equation is related to the curvature of the conduction and valence bands. The curvature dictates the overlap between carriers in the two bands; more overlap is found in material with more band curvature, or lower effective mass. More overlap between the conduction and valence bands causes higher B and increased recombination rate. Strain can be used to modify the effective masses in materials, which changes B. Not just band-to-band recombination produces radiative recombination; exitonic transitions [33] and Shockley-Read-Hall recombination can also be radiative, depending on the recombination centers [34].

A second recombination process, known as **Shockley-Read-Hall (SRH) recombination**, occurs because of the presence of trap levels in the bandgap. These

traps capture minority carriers to facilitate recombination. Energy is conserved by imparting the carrier's energy to lattice vibrations (phonons). Most SRH recombination occurs when the trap level is close or at midgap, because thermal emission quenches the SRH recombination for traps close to the band edges [32]. This is seen in the SRH rate equation:

$$R_{SRH} = \frac{\sigma_p \sigma_n v_{th} N_t [pn - n_i^2]}{\sigma_n \left[n + n_i exp\left(\frac{E_t - E_{mid}}{kT}\right)\right] + \sigma_p \left[p + n_i exp\left(\frac{E_{mid} - E_t}{kT}\right)\right]} \tag{2.3}$$

where σ_p (σ_n) is the capture cross section of holes (electrons) (cm^2), v_{th} is thermal velocity (cm/s), N_t is trap density (cm^{-3}), n_i is intrinsic carrier density (cm^{-3}), E_t is trap energy (eV), E_{mid} is the midgap (eV), k is Boltzmann's constant, and T is temperature. Notice that when E_t equals E_{mid}, the recombination rate becomes maximized. Also, this equation shows that increasing the capture cross sections, thermal velocity, trap or carrier extrinsic carrier density increases the recombination rates for the minority carrier. The SRH recombination rate A is dependent on material quality, and can be reduced by improving material quality [4].

Auger recombination is where a carrier recombines by imparting energy to another charge carrier which then dissipates the excess energy through phonons [32, 33]. Because this process involves interactions between carriers, it is highly dependent on carrier density, with recombination rates of:

$$R_a = anp + Cn^2 \tag{2.4}$$

for an n-type material and,

$$R_a = anp + Cp^2 \tag{2.5}$$

for a p-type material. In these equations, a represents energy transfer to the minority carrier and C is the energy transfer to the majority carrier. This recombination rate

is inherent to each material and cannot be improved by improving material quality. However, T2SL have been theoretically [26] and experimentally [1] shown to suppress Auger recombination.

Another way to think of a semiconductor surface is as a break in the periodic structure, which leaves dangling bonds. These bonds double as a range of midgap trap states as well as impurity getters [32, 33], causing **surface recombination**. **Interface recombination** is similar, but results from a junction of two bulk materials rather than a semiconductor-air interface. The surface recombination rate $R_{surface}$ is dependent on the surface recombination velocity S (cm/s), and the minority carrier density at the surface ρ_s (cm^{-3}) [32]:

$$R_{surface} = \rho_s S \tag{2.6}$$

where the surface minority carrier density is a function of the downward bending surface potential (V_s) and bulk density ρ,

$$\rho_s = \rho e^{-qV_s/kT} \tag{2.7}$$

and the surface recombination velocity depends on the majority carrier surface density N_{st}:

$$S = \sigma v_{th} N_{st} e^{-qV_s/kT} \tag{2.8}$$

While surface recombination is distinguished from the three main types of bulk recombination processes, it is nonetheless important for understanding experimental lifetime results and for experiment design. Electronic barriers made of materials with larger bandgaps can be used to separate surface recombination from bulk recombination by separating the surface from the bulk material.

Table 2.1: Reported lifetime measurements of T2SL and similar materials. NID is non-intentionally doped, and the various methods, photoconductive response (PCR), electron-beam-induced current (EBIC), current-voltage data fitting (IVF), optical modulation response (OMR), time-resolved differential transmission (TRDT), and time-resolved photoluminescence (TRPL) are described in Appendix A.

Reference	Year	τ (ns)	λ_{cutoff} (μm)	Doping	Method
Youngdale [35]	1994	0.13-6 at 77 K	8.8	NID	PCR
Yang [36]	2003	30 at 77 K	11.3	NID	PCR
		15 at 77 K	12.9	NID	PCR
		6 at 77 K	9.4	$3x10^{16}(p)$	PCR
Li [37]	2004	0.13 at 100 K	7.7	p-n jct.	EBIC
Pellegrino [38]	2009	35 at 77 K	LWIR	p-n jct.	IVF
Donetsky [39]	2009	80 at 77 K	4	NID	TRPL, OMR
Svensson [40]	2011	84, 92 at 77 K	4	NID	TRPL, OMR
Connelly [41]	2010	30 at 77 K	LWIR	p-type	TRPL
Donetsky [42]	2010	100 at 77 K	3.9	NID ($2x10^{16}$)	OMR
		31 at 77 K	10.3	$1x10^{16}$ (p)	OMR
Bandara [43]	2011	17	10	$5x10^{15}$	OMR
		32	10	$1x10^{16}$	OMR
		11	10	$2x10^{16}$	OMR
Olson [44]	2012	92 at 77 K	4.9	NID	TRDT
Zuo [45]	2013	48.4 (h), 50.8 (e)	10	p-n jct.	EBIC
		157 (h) , 70.3 (e)	11.8	p-n jct.	EBIC
Murray [46]	2014	58 - 82 at 77 K	4.4 - 5	NID	TRPL
Steenbergen [47]	2011	412 at 77 K	8.2	NID ($3x10^{16}$)	TRPL
Olson [44]	2012	9,000 at 77 K	5.4	NID	TRDT

2.4 T2SL and constituents' lifetimes

InAs/GaSb type-II superlattice has proved to be both successful at Auger recombination suppression and disastrous due to its large Shockley-Read-Hall recombination. Initially, T2SL seemed advantageous for its Auger recombination suppression. However, material lifetime measurements revealed low lifetimes in T2SL due to SRH recombination. Table 2.1 lists reported T2SL minority carrier lifetimes, showing that T2SL lifetimes were found to be short (100 ns at most), regardless of doping level or type, institution of growth, cutoff wavelength, or characterization technique.

Within these references, insights into the low lifetime problem are provided. Three

groups reported on the relative energy of the trap within the bandgap. Yang [36] used electroluminescence to measure this and found them to be ∼1/3 of the bandgap (E_g) from the conduction band edge in a 9 monolayer (ML) InAs / 5 ML GaSb T2SL. Connelly reported a trap 20 meV above the valence band in LWIR samples [41] and in a different publication a trap 60 ± 15 meV above the valence band for MWIR samples ($E_g \sim 250$ meV) [48]. These results show that the energetic location of detected trap levels varies, which may vary by the cutoff wavelength of the material.

Other lifetime studies have hypothesized specific causes of the traps and attempted to increase the lifetime from these guesses. An extensive study by Svensson [40] targeted both the interfaces and growth temperature as possible causes of SRH recombination. By measuring the lifetime as a function of T2SL interfaces per volume, it was assumed a variation in lifetime would point to interfaces as the cause of low lifetimes. However, no correlation was found between lifetime and interfaces per volume, indicating that interfaces were not the culprit. Intriguingly, their study also found that the optimum growth temperature for T2SL produces similar lifetimes in bulk GaSb (∼ 50 ns), as in T2SL, but not InAs (∼ 250 ns). They observed that increasing the growth temperature of the GaSb increased its carrier lifetime, from ∼50 ns at 440°C to 150 ns at 510°C. The authors also pointed out that if higher T2SL growth temperatures were possible without reducing the coherence of the T2SL, higher lifetimes might be achievable. A separate study of different interface combinations (samples with and without Sb and As soaks at interfaces) by Murray [46] found that interface roughness is not the cause of SRH recombination in T2SL, in agreement with Svensson's conclusion that interfaces are not responsible for reduced lifetime. However, a report by Zuo [45] found that carefully chosen thickness of the InSb strain compensation layer increases the hole lifetime in n-doped regions (but the electron lifetimes were unchanged), which is somewhat contradictory of Murray and Svensson's conclusions. Murray [46] also investigated the effect of growth rate on T2SL

lifetime, and found a maximum lifetime of (82 ns) for InAs and GaSb growth rates of 0.5 monolayers per second. Therefore, even though optimal growth rates exist, they do not allow for significant improvements.

The last two references in Table 2.1 report on InAs/InAsSb (Ga-free) superlattice lifetimes. In 2011, a breakthrough in carrier lifetime for type-II superlattices happened; by replacing the GaSb layers with $InAs_xSb_{1-x}$, carrier lifetimes were increased by over an order of magnitude [44, 47]. This result implied that the low lifetimes in InAs/GaSb superlattice are related to the presence of gallium, and sparked an interest in Ga-free T2SL. Indeed, based on Svensson's [40] observations of low lifetimes in bulk GaSb grown at T2SL temperatures, it seems possible that the low growth temperatures crystallographically optimal for T2SL (approximately 400 °C) are deleterious for its GaSb layers (optimally grown at 500 - 550 °C). Both T2SL and Ga-free superlattices are grown on GaSb substrates [47] and can have similar layer thicknesses [44]. Unlike T2SL, Ga-free superlattices with long lifetimes did not require any specific strain compensation layer or interface control, the InAsSb was not lattice matched to GaSb, and in Ga-free superlattices each layer has indium as a cation, rather than having gallium and indium in alternating layers.

From the literature, it is apparent that optimizing the lifetime of T2SL depends partially on optimizing the carrier lifetime of GaSb at low growth temperatures. However, because of the conflicting data of Murray [46], Svensson [40], and Zuo [45] it is not possible to rule-out interfaces as a potential for improvement as well. Part of the reason for conflicting data over the interface issue arises because "interfaces" is a broad term. It could refer to either the junction between the InAs and GaSb layers (eg. GaAs-like or InSb-like interfaces), or diffusion of atoms between these layers and prevention of this diffusion through proper interface growth.

There are several types of defects that could be responsible for the SRH recombination in superlattices:

1. Impurities / doping atoms
2. Inter-diffusion of layers
3. Interfaces
4. Constituent material (GaSb)

Impurities, either intentionally added to the sample or unintentionally from the growth chamber or subsequent processing steps, can contribute to SRH. Defects such as substitutionals or antisites (substitute the incorrect atom in place of the correct one), vacancies (atom is missing), and interstitials (atom out of place from the crystallographic order) can also form, either with native atoms or impurities [49]. Often, these defects appear in complexes, such as a vacancy and an antisite pair, for example. Some defects are mobile during growth [50], while others are mobile during regular device operation. Defects can be either deep or shallow, which defines whether or not they contribute to SRH recombination. A shallow defect is near the band edges and is easier to ionize, while a deep level lies near midgap. Because of thermal emission, a shallow defect is rendered innocuous; any trapped carriers can escape with extra energy from thermal emission [32]. Deep levels are too far from either band to allow carriers to escape through thermal emission. A defect thought to be responsible for GaSb's propensity to be residually p-type is the $V_{Ga}Ga_{Sb}$ (Ga vacancy and Ga on Sb site) complex [51].

Previous work allows us to chose what aspects to target for increasing T2SL lifetime. Many studies have focused on the interface control, with limited success. Few, however, have examined how the constituents effect lifetime, in spite of the growing evidence that GaSb has an important role in lifetime reduction. This project did explore different interfaces and their impact on lifetime, but most of the focus is on GaSb for use in T2SL. Before diving into the details of this study in chapters 4

and 5, basic growth, fabrication, and characterization techniques used in this work are covered in the following chapter.

Chapter 3

Sample Growth, Fabrication, and Basic Characterization

3.1 Growth

Molecular beam epitaxy (MBE) is a growth method in which molecular beams of material impinge on a substrate in ultra-high vacuum. Shutters covering the sources allow the user to finely control the growth thickness atomic layer by layer. While a sample is growing, the growth rates are calibrated and surface quality is monitored by reflection high energy electron diffraction (RHEED). Each epitaxial layer needs specific growth temperatures and flux ratios, which depend on what elements the epitaxy is composed of. In addition, InAs/GaSb superlattice has stringent requirements on InAs and GaSb layer thickness to control the bandgap, as well as interface growth and composition to control layer intermixing and strain.

All samples discussed in this dissertation were grown in a VG-80 MBE system with Ga and In SUMO sources and group V valved crackers to supply Sb_x and As_x. Our reactor grows III-V semiconductors, meaning that at least one element from column III and from V of the periodic table are used simultaneously during growth.

Epitaxy-ready substrates, such as GaSb, GaAs, or InAs, bought from a manufacturer, are mounted on Mo plates and loaded into the machine through a load lock. These substrates are then transferred to the preparation chamber which is under UHV, where they are baked to remove any impurities such as water vapor.

After the bake, the substrates are moved to the main growth chamber, which has heated III-V sources, shutters to cover the sources, pumps such as a liquid nitrogen shroud, a cryo-pump, and an ion pump, ion gauges, a residual gas analyzer (RGA), and a reflection high-energy electron diffraction (RHEED) gun. The pumps keep the chamber pressure in the 10^{-10} mBar regime; the liquid nitrogen shroud encompasses the substrate to capture impurities before they can come in contact with the substrate. An RGA is used to monitor the composition and relative quantity of molecules within the chamber.

To control growth rates, the sources are heated up to specific temperatures and maintained to within 0.1 °C with proportional-integral-differential (PID) controllers. Group V material initially sublimates into As_4 and Sb_4. To crack these molecules into a more useful form, the tip of the source crucible (nearest to the growth chamber) are heated 400-500 °C more than the base (furthest from the growth chamber) where the group V material is. These high temperatures break the As_4 and Sb_4 molecules into As_2 and Sb_2 or Sb_1. Using cracked group V material has the advantage of increasing the range of substrate temperatures such that the crystalline quality is still high. The Ga source also has a higher tip temperature than base temperature, in order to prevent droplets of Ga from forming around the mouth of the source and falling back into the liquid gallium at the base, causing splashing or spitting on the epitaxy's surface.

Each source opens into the main growth chamber, pointing at the substrate. Molecular beams are formed by heating high-purity ("7N" or 10^{15} background doping) elemental material in pyrolytic boron nitride (PBN) crucibles, whose openings

face the substrate. Parts that are heated within the chamber are made of materials such as PBN, molybdenum, or tantalum that do not introduce as many unwanted materials to the chamber. To control which beams are impinging on the substrate and when, mechanical shutters cover or reveal the source mouth. Because the growth rates are slow (less than 3 Å/s) the growth thickness can be controlled to within fractions of an atomic layer by shutter timing.

An ion gauge is present that can move into the exact location of the substrate. This is used to measure the flux of molecules coming from each source and is especially useful for measuring flux ratios, the ratio of one source's flux to another (group V/group III). Flux ratios are important because if there is too much or not enough of one material relative to another, defects can form. Prior to growth, flux ratios are optimized by fixing the group III fluxes and varying the group V fluxes through valves at the crucible opening. Typical flux ratios for growth are given in Table 3.1.

Substrates grown by the Czochralski method arrive from the manufacturer as "epi-ready", implying that the grower does not need to prepare the substrate prior to loading it into the MBE. These substrates are covered with a passivating layer of oxide, introduced by the substrate manufacturer. The oxide reduces carbon contamination of the substrate when it is exposed to the atmosphere [52]. Once a substrate has been loaded into the growth chamber, it is heated while under group V flux to remove these oxides prior to growth. A list of oxide desorption temperatures for various substrates is given in Table 3.1. The progress of the oxide desorption is observed with a RHEED system, in which electrons (from an electron gun directed at the substrate) are diffracted by the crystal onto a phosphor screen. When an oxidized substrate is present, the RHEED screen reveals a few spots or no features at all, but when the oxide is removed, spots and streaks appear.

After oxides are desorbed, the substrate temperature is reduced to a desired growth temperature. This temperature is highly dependent on what the epitaxial

layer will be (see Table 3.1 for select growth temperatures). Then, the source shutters open and molecules interact with the substrate to form an epitaxial layer. If the growth does not go well, streaks will disappear or blur and more spots will form, indicating that the surface is becoming rougher. If the growth is successful, the diffracted RHEED pattern shows the dots and few streaks of the oxide-desorbed surface gradually change to long streaks. RHEED is also used to calibrate group III growth rates. This is done by monitoring the intensity of the diffraction spots with time. When a layer of molecules begins to grow, the surface has only patches of molecules, which makes it slightly rough and the spot dim. Then, as the molecules begin to fill in the layer, the spot brightens again. This process repeats as single layers of the material grow, causing the spot intensity to oscillate. These oscillations are monitored with a camera, to measure the growth rate.

The temperature of the substrate is measured by a pyrometer during growth. However, this pyrometer has a limited range, and cannot determine sample temperatures less than ∼440°C. Other means of determining substrate temperature are used instead, such as the RHEED reconstruction transition, where the RHEED pattern of GaSb switches from a 1x3 pattern to a 1x5 pattern [53]. In our MBE, this transition happens at about 425°C. InAs/GaSb superlattice is grown at approximately 400°C (or 25°C below the RHEED reconstruction transition temperature) and has flux ratios of 4 for Sb/Ga and 4 to 9 for As/In. Before the main structure is grown, a layer of the same material as the substrate (GaSb) is grown. This helps prepare the substrate by making a smooth, high-quality crystalline layer. Then the superlattice is grown. Each period of the superlattice is made of several layers of material (as shown in Figure 2.1), including an InAs layer, one interface, a GaSb layer, and a second interface. The thickness of the InAs and GaSb layers dictate the bandgap of the superlattice, while the interfaces are used to manipulate strain and reduce atomic mixing of the separate layers. Because InAs and GaSb have different lattice constants, strain forms as the

Table 3.1: Growth recipes for T2SL and its constituents

Material	T_{oxide}	T_{growth}	V/III flux ratio	References
InAs	520-540	440-520	12-18	[54, 55, 56, 57]
GaSb	530-540	500	4-5	
GaAs	650	600	10-12	
T2SL	NA	$\sim$ 400 ($T_{transition}$−25 to 45°)	Sb/Ga = 4 As/In = 4-9	[58]

superlattice grows. To compensate for the smaller lattice constant of InAs (a_{InAs} = 6.058 Å), an InSb layer (a_{InSb} = 6.47 Å) is grown between the GaSb and the InAs. The required InSb layer thickness is calculated by considering lattice mismatch:

$$\Delta = (a_1 - a_2)/a_2 \tag{3.1}$$

where a_1 denotes lattice constant of material the epitaxy and a_2 is the lattice constant of the host material. Using this equation for both the InAs and InSb lattice mismatch with respect to GaSb leads to a required InSb thickness of:

$$d_{InSb} = d_{InAs}(a_{InAs} - a_{GaSb})/(a_{InSb} - a_{GaSb}) = 0.098 \times d_{InAs}. \tag{3.2}$$

If strain compensation is not possible, a mismatched layer can be grown as long as it does not exceed the critical thickness (h_c), the maximum thickness an epitaxial layer of one lattice constant (a) can be, when grown on a crystal of different lattice constant (a_o), before excessive strain causes defects to form:

$$h_c \approx a^2/[2(a_o - a)] \tag{3.3}$$

Table 3.2: Photoresist recipes. Notes: a) post-exposure bake at 112°C, flood exposure for 30 s. b) follow with five minute air dry and edge bead removal. c) perform edge bead removal after spin. d) follow with post-exposure bake of 95°C for 130 s.

Photoresist	Spin (RPM)	Bake (time / temp)	Exposure (s)	Develop (s)
AZ4330	5000	90 s / 90°C	5.4	70 (AZ400K 1:4)
AZ5214-IR	5000	90 s / 90°C	1.9[a]	35 (AZ400K 1:5)
AZ4620	3000[b]	60 s / 90°C	30	390 (AZ400K 1:4)
SU-8 2002	3000[c]	60 s / 95°C	2.3[d]	45 (SU-8 developer)

Table 3.3: Plasma etching. The sample temperature is fixed at 25°C.

Recipe	Gas / Flow	RF Power	ICP Power	Chamber Pressure
Zia-InP	BCl_3 / 35 sccm	90 W	500 W	2.5 mTorr

3.2 Fabrication

Fabrication describes the process of creating features on a semiconductor wafer, and can include such steps as an etch to make electrically isolated devices, metal deposition to create electrical contacts, or dielectric deposition to electrically passivate the semiconductor surface. Each of the steps is associated with a mask, which is a piece of glass with metal patterns on it. In each fabrication step, a layer of photoresist (a light-sensitive material, see Table 3.2 for more specific photoresist recipes) is applied to the sample, the sample and mask are aligned, and then the sample is exposed to UV light through the mask. This exposure transfers the pattern of the mask onto the sample, by causing a chemical reaction in only the exposed parts of the photoresist. Then, the sample is developed to remove the unwanted parts of resist and to retain the desired pattern. There are several processes that can be done on a patterned sample, such as etching, metal deposition, or passivation.

Etching the sample removes sections of the sample to define electrically isolated devices. This can be accomplished with either wet (acid) or dry (plasma) etching. Plasma etching was used for all of the work in this dissertation. Table 3.3 shows recipes used for various material etching.

Two kinds of mask sets were used for the characterization described in this dissertation, a single-pixel photodiode mask set and a Schottky diode mask set. The single pixel mask was developed by another student and consists of 410 x 410 μm square mesas with apertures of 300 μm, 200 μm, 150 μm, 100 μm, 50 μm, and 20 μm. There is also a set of square mesas with variable area dimension, without apertures, with sides of 400 μm, 300 μm, 200 μm, 100 μm, 50 μm, and 30 μm long. The steps for this mask set are: 1) mesa delineation with AZ4330 photoresist feature definition followed by inductively coupled plasma (ICP) etching with BCl_3 (Zia-InP recipe), 2) metal deposition with AZ5214-IR photoresist feature definition, followed by a 30 s acid dip (1 HCl : 10 H_2O), and metal deposition of 500 Å Ti, 500 Å Pt, 300 Å Au, 3) 30 s acid dip (1 HCl : 10 H_2O) followed by passivation with SU-8 2002. After SU-8 is applied, the sample is baked at 175°C for 30 minutes to solidify the SU-8. The acid dip steps are used to remove native oxides from the surface where metal or passivation will be applied.

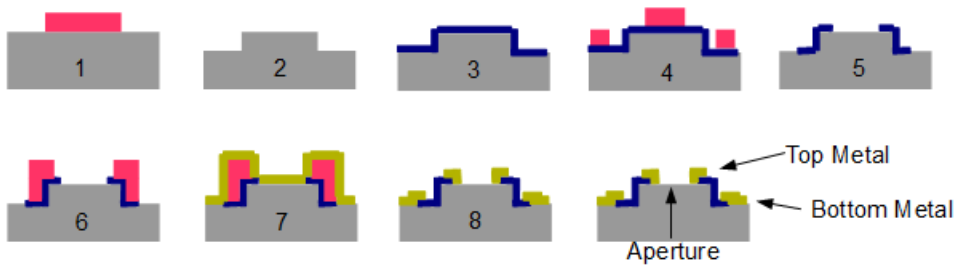

Figure 3.1: Process steps for single-pixel diode mask. 1) Mesa lithography, 2) mesa etch, 3) SiN_x passivation, 4) passivation etch mask, 5) passivation etch, 6) metal lithography, 7) metal deposition, 8) metal liftoff.

The Schottky diode mask set, shown in figure 3.3, was developed specifically for this project, and consists of inter-digitated mesas of various areas. Each finger is 100 μm wide, with an 80 μm-wide top contact. The width of the mesa was chosen based on lateral diffusion data of T2SL [59]. This mesa was defined with AZ4330 and etched with the Zia-InP ICP recipe. After this a 50 Å layer of SiO_2 was applied,

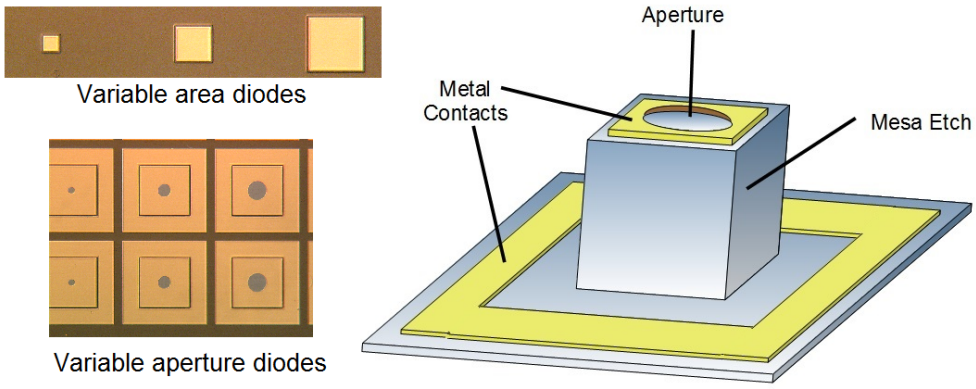

Figure 3.2: Left: Single-pixel diode microscope images of variable area and variable aperture diodes. Right: structure of a variable aperture device.

to help improve the quality of the Schottky diode. There is also an optional layer that makes a dielectric ring, which prevents leakage and breakdown effects near the edges of the metal. Next are two metal layers that are deposited in separate steps, 1) a wirebonding pad, and 2) a thin metal that forms the Schottky barrier and allows for light transmission. The wire bonding pad was defined by AZ5214-IR photoresist, then native oxides were removed with a 30 s acid dip (1 HCl : 10 H_2O), and then 500 Å Ti / 500 Å Pt / 1000 Å Au is deposited. After liftoff, the sample is again dipped in the HCl acid solution for 30 s, and then 150 Å of Au is deposited. After this liftoff, the sample is complete.

3.3 Photoluminescence spectroscopy

Photoluminescence occurs when above bandgap photons incident on a sample are absorbed. This promotes electrons from the valence band to the conduction band or to a trap level. The electrons that return to the valence band through radiative recombination will then emit a photon, which has an energy equal to that of the energy lost by the electron during recombination (approximately the band gap energy). This technique allows for measurement of the band gap of the material. It can

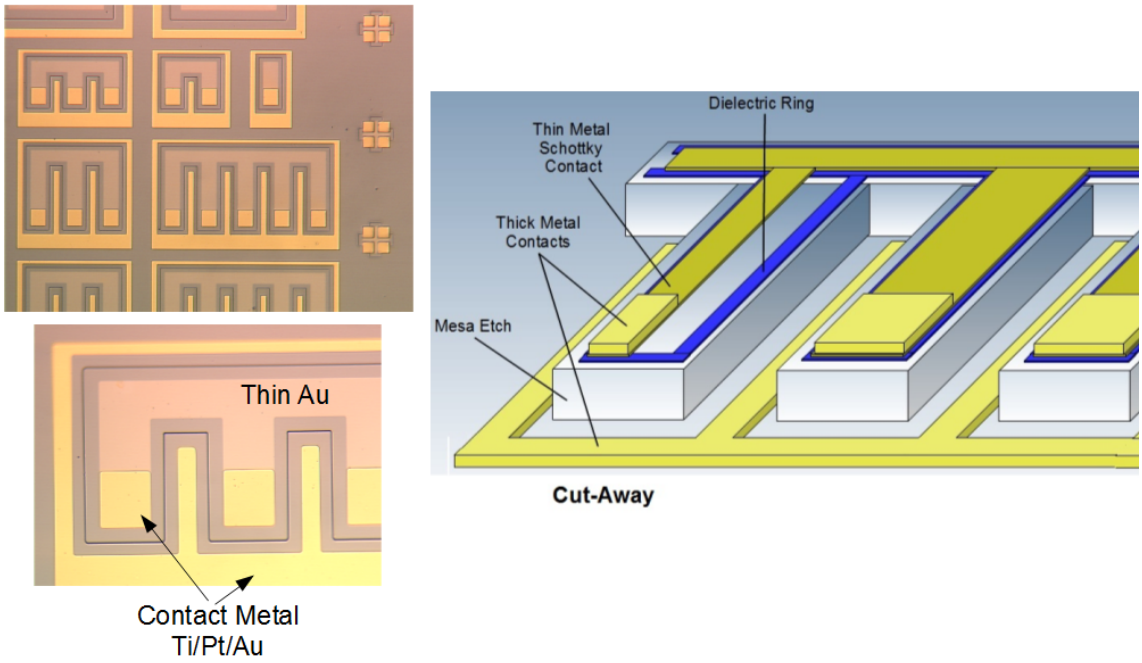

Figure 3.3: Schottky diode mask microscope images and structure.

also be used to compare material quality, which is measured, roughly, by the intensity of the PL as well as its full-width-half maximum. The reason the PL intensity cannot be correlated directly with defect densities is because there are several types of recombination that contribute, including surface recombination [49]. To compare the intensity of different samples, the measurements should be made consecutively, in the same characterization session, and without changing the alignment of any of the optics. This makes the data more comparable, though there are still intensity variations expected over the area of each sample.

A schematic of the PL setup is shown in figure 3.4. The light from either a HeNe (632 nm) or Argon (514 nm) laser is directed through a chopper (spinning at ~215 Hz) and is focused onto the sample. The PL from the sample is then collected by a lens (CaF_2) and directed and focused onto the entrance slit of a monochromator. A diffraction grating within the monochromator is used to select an output wavelength, which is then directed through the monochromator's exit slit and onto a detector

(InSb, operational from 1-5 μm). The detector measures the PL intensity for the selected wavelength, and sends that signal to a lock-in amplifier, which locks on to the frequency specified by the chopper. This means that it discards any signal that doesn't have a frequency matching in the chopper frequency, using only the ones that match. This signal intensity is then sent to a computer which saves and plots the data. Often, the light entering the monochromator is filtered so that light from the laser beam is not accidentally measured.

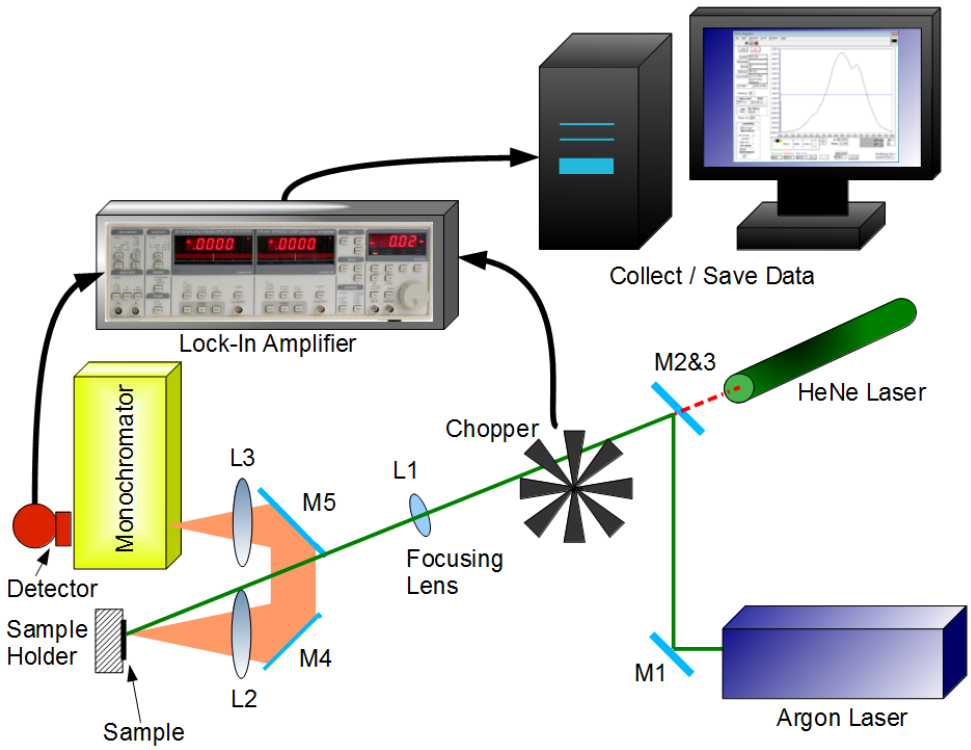

Figure 3.4: Diagram of photoluminescence setup. Light from either the argon or HeNe laser is directed through an optical chopper and focusing lens, and onto the sample. The sample absorbs the laser light, and then re-emits photons at a wavelength corresponding to its bandgap. This light gets collected and directed by lens 2 and 3 and mirror 4 and 5 to the monochromator. The monochromator scans through a requested wavelength range, and the intensity at each wavelength is measured by the detector. The detector signal and the frequency of the chopper are sent to the lock-in amplifier, which measures the intensity of signals only if they have the same frequency as the chopper. This intensity information is then sent to a computer which plots the PL intensity verses wavelength.

Chapter 4

Time-Resolved Photoluminescence for Interface and Doping Effects on Lifetime

Many causes of SRH recombination in T2SL have been suspected, and can be generalized under three main categories: interfaces, low growth temperature, and layer mixing. Our research group had previously examined five interface recipes and compared them using PL intensity as a metric [60]. Of these five, the three best recipes were chosen for the interface study described in this chapter, where the lifetimes of these recipes are compared using time-resolved photoluminescence. The motivation was to be able to recommend an interface recipe that would promote the longest carrier lifetimes. Another aspect that would not be expected to drastically improve carrier lifetime, but rather is an essential component in most detector structures is the doping. The type of dopant atom, Be or Te, as well as its placement within the T2SL, GaSb layer, InAs layer, or both, is examined for its effect on carrier lifetime. First, an overview of TRPL is given, for both the underlying physics and a walk-through of the experimental setup used in this study. Then, the experiment and results are

discussed for the doping and interface studies.

4.1 Physics of TRPL

Time-resolved photoluminescence (TRPL) is a time-domain measurement technique in which the photoluminescence (PL) intensity decay of a sample is collected as a function of time to measure directly the carrier lifetime [41, 39, 32, 61]. The sample architecture in this measurement is designed to minimize the effects of surface recombination, with aluminum-based layers (typically AlSb or AlGaSb) sandwiching the material of interest, that segregate the bulk material from the surface. This measurement is performed in the time domain instead of the frequency domain. Pulsed laser light incident on the sample, with greater energy than the bandgap, excites electrons to the conduction band. The electrons "live" in this excited state for some time before recombining with holes in the valance band, emitting photons as a result (photoluminescence). The emitted photons are directed to a detector, which measures the PL intensity as a function of time. The carrier lifetime is then determined by fitting an exponential decay model to the intensity measurements. For simple decays, where carrier injection is low and SRH recombination dominates, the exponential decay model is:

$$I_{PL}(t) = e^{-t/\tau_{minority}} \tag{4.1}$$

Where $\tau_{minority}$ is the minority carrier lifetime. For high carrier injection conditions the model is adjusted to:

$$I_{PL}(t) = e^{-t/(\tau_{minority}+\tau_{majority})} \tag{4.2}$$

where $\tau_{majority}$ is the majority carrier lifetime. For more complex PL decay this

Table 4.1: Commonly employed T2SL minority carrier lifetime measurement techniques, including photoconductive response (PCR), electron-beam-induced current (EBIC), current-voltage fitting (IVF), optical modulation response (OMR), time-resolved differential transmission (TRDT), and time-resolved photoluminescence (TRPL).

Method	Assumptions	Direct	Indirect	Time Dom.	Freq. Dom.	Steady-State
PCR			X			X
EBIC	$\mu_{e,h}$		X			X
IVF	$\mu_{e,h}$, m*, N_T		X			X
OMR		X			X	
TRDT	α	X		X		
TRPL		X		X		

model is extended to [41]:

$$I_{PL}(t) = B\delta n_{t=0}^2[e^{-2t/\tau} + (p/\delta n_{t=0})e^{-t/\tau}] \tag{4.3}$$

where B is the radiative recombination coefficient, $\delta n_{t=0}$ is the initial carrier injection level, p and n are the electron and hole background densities, and $I_{PL}(t)$ is the time-dependent PL intensity. TRPL is a direct measurement of carrier lifetime with no assumptions; it is a very reliable method for determining carrier lifetime.

For a description of other lifetime measurement techniques, refer to Appendix A. A comparison of the different lifetime measurement techniques is presented in Table 4.1. Direct methods that make zero to few assumptions about the sample and fitting process are the most reliable. Current - voltage fitting (IVF) and electron beam induced current (EBIC) use assumed values to fit a mathematical model to data, making these methods dubious, while optical modulation response (OMR), time-resolved differential transmission (TRDT) and TRPL are more reliable. Another advantage of OMR, TRDT, and TRPL is that these measurements are performed on unfabricated samples, eliminating the effects of processing uncertainties from the resulting lifetimes.

4.2 Time-Resolved Photoluminescence Setup

Following the discussion of the basic principles of a time-resolved photoluminescence measurement from Section 4.1, the specific setup used to perform TRPL measurements can now be addressed (please follow figure 4.1 for reference). All lifetime measurements were performed at Army Research Lab in Adelphi, MD. Each sample was mounted in a cryostat with a temperature range of 8 - 300 K. PL was excited using a 2 μm wavelength laser with a 100 fs pulse width and a 250 kHz repetition rate. The intensity of this source (and thus carrier injection levels) was controlled using various neutral density filters. Injection intensities corresponded to initial carrier densities of $7.3 \times 10^{16}, 3.6 \times 10^{16}, 2.1 \times 10^{16}, 1.1 \times 10^{16}, 5.5 \times 10^{15}, 3.1 \times 10^{15}, 1.6 \times 10^{15}, 1.0 \times 10^{15}$, and 5.1×10^{14} cm^{-3}. To calculate initial carrier injection (δn_0), the incident power (P, 1 mW maximum), absorption coefficient (α, 2000 cm^{-2}), epitaxial layer thickness (d, 2 μm), sample reflection coefficient (R, 2%), photon energy from the laser (E_{photon}, 0.62 eV), laser beam area (A_{beam}, 1×10^{-5} m^2), and repetition rate of the pulsed laser beam (r, 250 kHz) were used:

$$\delta n_0 = Pd(1 - e^{-\alpha d})\frac{1 - R}{E_{photon} A_{beam} r} \tag{4.4}$$

Off-axis parabolic mirrors were used to collect and direct the PL signal onto a HgCdTe detector, which had a maximum cutoff wavelength of 10 μm and a minimum response time of 3 ns. The signal from the detector was sent through an amplifier and sent to a data acquisition system. To improve the signal-to-noise ratio and the reliability of the measurement, several decay plots were collected and averaged.

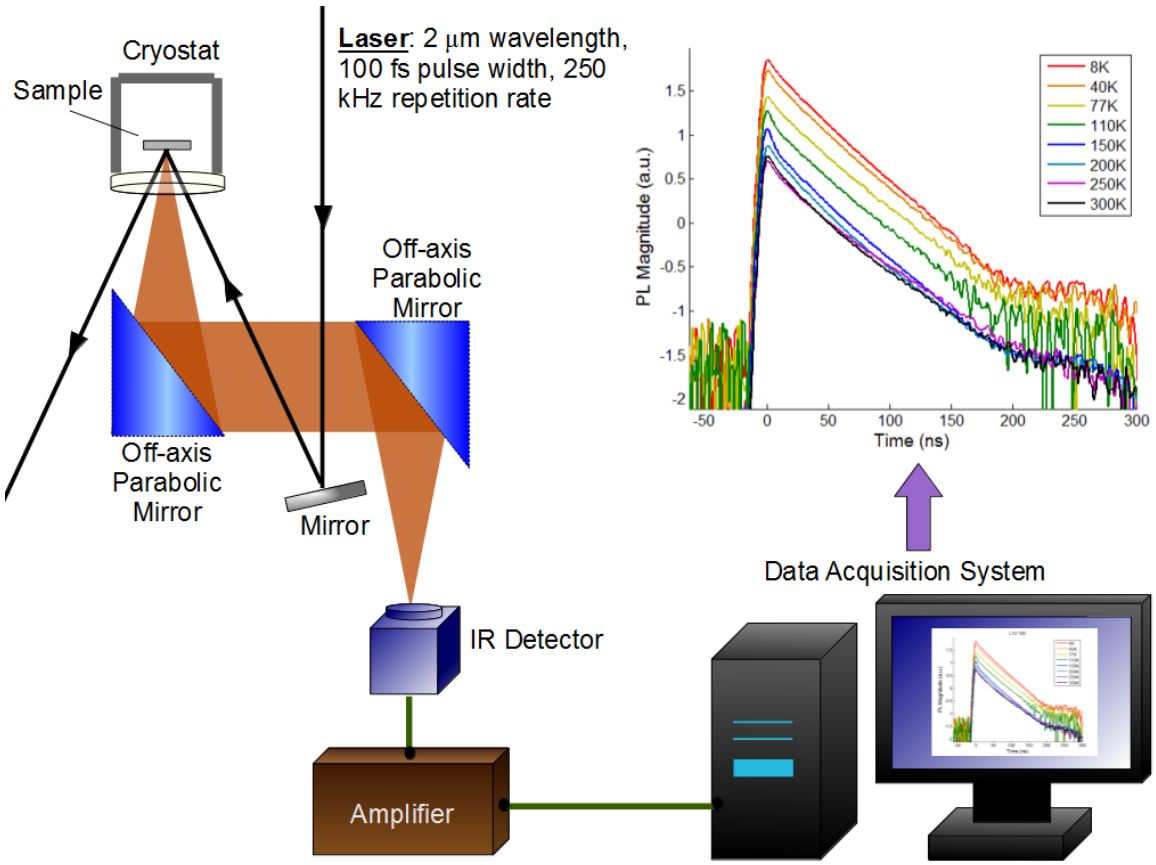

Figure 4.1: Diagram of TRPL setup. A laser beam is directed onto the sample held within a cryostat. The resulting photoluminescence is collected by off-axis parabolic mirrors, and concentrated onto an IR detector. The signal from the IR detector gets amplified, and is recorded on a data acquisition system. A representative plot of the resulting TRPL decay plots is shown for a wide range of temperatures.

4.3 Minority Carrier Lifetime Measurements of T2SL

All samples grown in this study used the basic growth process outlined in section 3.1. The universal structure used for this study consisted of 6 layers (see figure 4.2): 1) GaSb Te-doped substrate, 2) a ~500 nm smoothing layer, 3) a 10 nm AlSb electrical barrier, 4) a 2 μm thick 8 ML InAs / 8 ML GaSb superlattice region-under-test, 5) a second 10 nm AlSb electrical barrier, and finally 6) a 5 nm GaSb capping layer to prevent oxidation of layer 5. Note that the 10 nm of AlSb was far below the cal-

culated critical thickness (48 nm) of AlSb on GaSb (from equation 3.3). Empirical pseudopotential modeling (code courtesy of Nutan Gautam) was used to calculate the relative band alignments of the different layers to confirm that the AlSb layers acted as barriers to both electrons and holes. If they did not act as barriers, surface recombination would dominate the TRPL measurement, producing much lower lifetimes than the bulk lifetimes of interest. Using this architecture in conjunction with the described TRPL setup, two different investigations were undertaken: 1) a doping study to determine if doping atom element or placement impact lifetime, and 2) an interface study where different growth sequences were used to form different interfaces to determine if an optimal interface recipe with long lifetimes could be found.

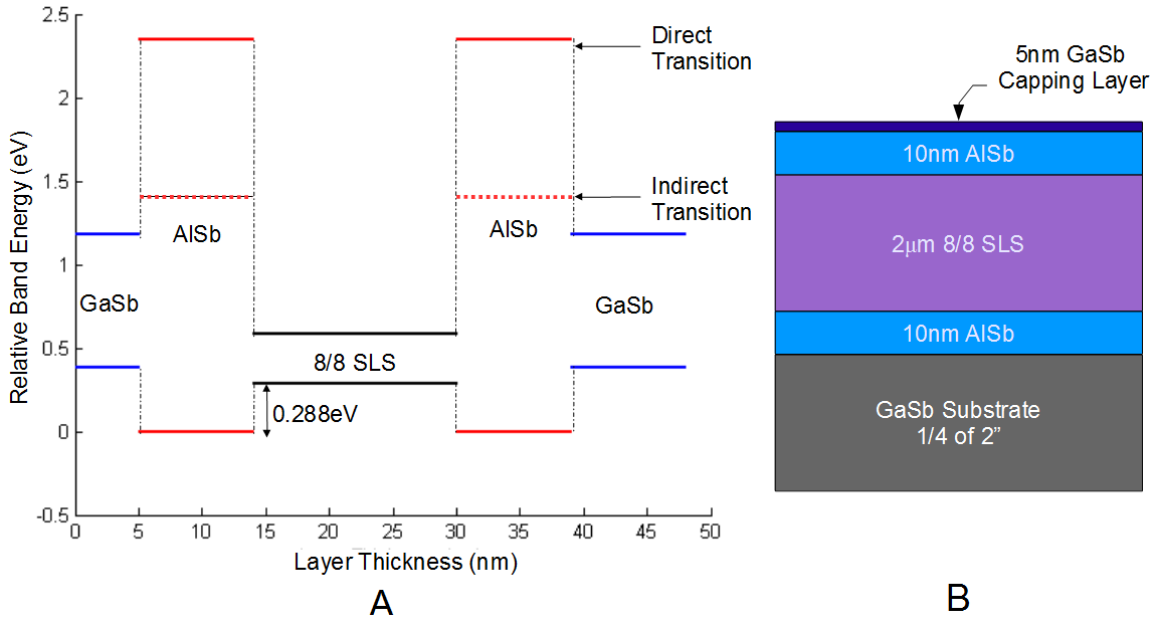

Figure 4.2: Universal structure used in all TRPL experiments discussed in this work: A) relative band energies calculated by empirical pseudopotential method (code courtesy of Nutan Gautam), which shows that the AlSb layer acts as a barrier for both electrons and holes, B) illustration of sample layers and thicknesses (smoothing layer of GaSb between substrate and AlSb not shown).

Table 4.2: Measured lifetime of doping study samples at different temperatures and injection conditions: low-injection (1 to 5 x10^{15} cm^{-3}) and high-injection (7.3 x10^{16} cm^{-3}).

	Layer	A	B	C	D	E	F	G
	InAs	NID	Te	NID	Te	Be	NID	Be
	GaSb	NID	NID	Te	Te	NID	Be	Be
Injection	Temperature (K)	τ (ns)						
Low	8	49.4	3.1	$\leq$3	$\leq$3	12.2	11.7	12.8
	77	48.5	$\leq$3	$\leq$3	$\leq$3	14.8	11.6	9.4
	300	47.9	NA	NA	NA	44	34.3	33
High	8	37.7	13.9	8.4	$\leq$3	35.4	33.6	29.1
	77	36.3	16.2	8.4	3.1	38.2	34.7	29.7
	300	39.2	NA	NA	NA	38.9	37.2	31.6

4.3.1 Doping Study

Seven samples were grown for the doping study named samples A-G in table 4.2. In the table, below the name of each sample, is the corresponding layer (InAs and GaSb layers) doping, either non-intentionally doped (NID), Te-doped, or Be-doped. Each sample was grown at $\sim$ 25°C less than the RHEED transition temperature from a 1x3 pattern to a 1x5 pattern [53]. Growth rates of 0.23 ML/s for Al and 0.48 for Ga and In were used. The growth sequence for each superlattice period was: 1) 8 ML of InAs, 2) 0.6 s Sb soak, 3) 8 ML GaSb, 4) 0.5 ML InSb (1 s).

After growth, the samples were characterized with x-ray diffraction and photoluminescence. The XRD results, with a representative plot shown in figure 4.3A, had an average percent mismatch for the 0^{th} order satellite T2SL peak to the substrate peak of 1.2% (compressive), and the 0^{th} order peak had a full-width half-maximum of 44 arc-seconds. Room-temperature photoluminescence, shown in a representative plot in figure 4.3B, had oscillations which we have attributed to Fabry-Perot resonance. There is also a notch at $\sim$4.2 μm, which is due to CO_2 absorption of the PL. This spectrum, while broad compared to other materials, is typical of a T2SL. All samples had similar intensities, roughly on the same order of magnitude.

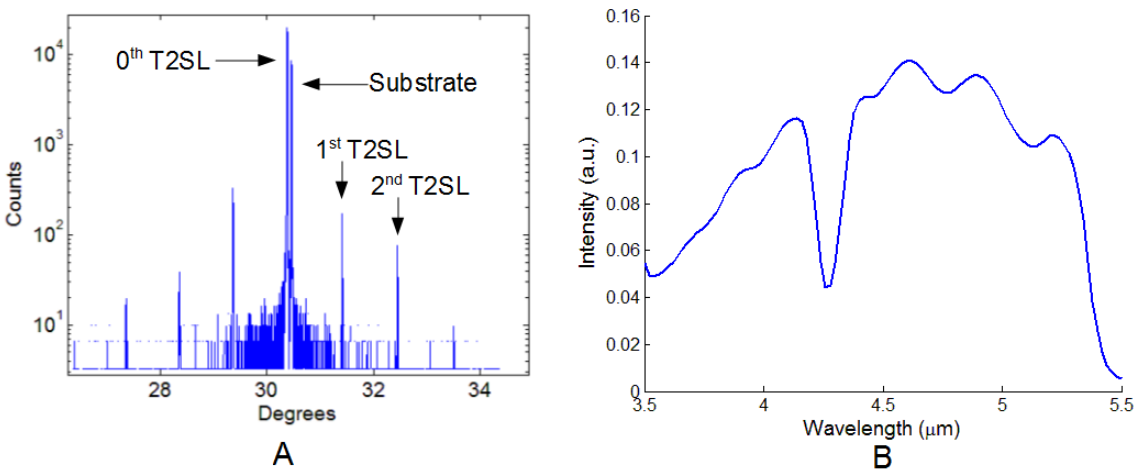

Figure 4.3: Representative plots of the A) XRD data and B) photoluminescence spectrum of samples from the TRPL studies.

From the lifetime values in table 4.2, it is apparent that lifetime does depend on the type of dopant. Te-doped samples showed the lowest lifetimes (around 3 ns at low injection), regardless of which layer was doped, Be-doped showed increased lifetimes (10-40 ns at low injection), and the control (NID) samples showed the highest lifetimes (∼48 ns). The effects on lifetime of doping different layers is illustrated in figure 4.4, which shows that whether Te or Be are used, doping the InAs layer produces marginally (∼5 ns) longer lifetimes.

Trap saturation [61], which happens when the SRH capture rate of the majority carrier is slower than the capture rate of the minority carrier, was observed in the Be- and Te-doped samples. Trap saturation manifests as a bowing in the TRPL plots (see figure 4.5 for example). The reason this is significant is that for high injection levels, the injected carrier density (I) decays by the sum of the minority and majority carriers [61]:

$$I(t) = e^{-t/(\tau_{minority}+\tau_{majority})} \tag{4.5}$$

rather than simply as the minority carrier, which is seen for low injection levels:

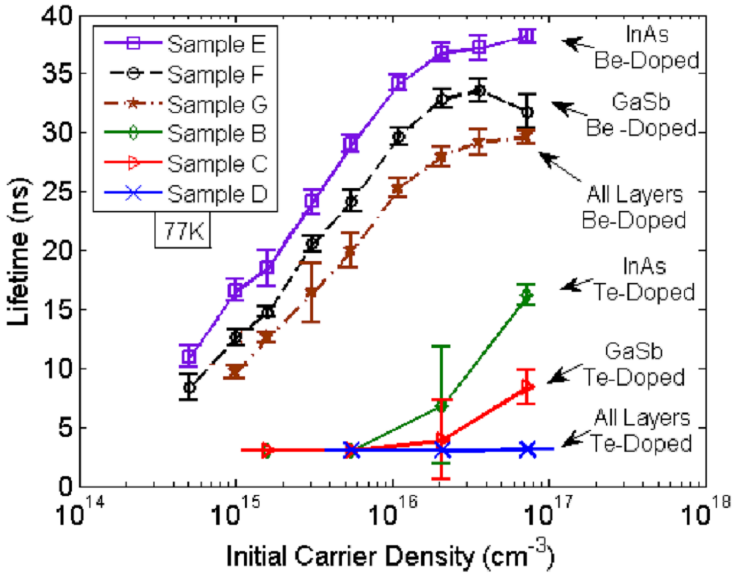

Figure 4.4: Lifetimes of the doping samples at 77K for different injection levels. From reference [62].

$$I(t) = e^{-t/\tau_{minority}} \tag{4.6}$$

The transition from the high-injection regime, where the majority and minority carriers play a role, to the low-injection regime, where the minority dominates, causes the bowing in the time-resolved PL decay in figure 4.5A. Therefore, any lifetime information extracted from a decay plot that has this bowing is not strictly the minority carrier lifetime, but is more likely a combination of both the majority and minority lifetimes. This means that what is referred to as low-injection data provides a more realistic representation of the minority carrier lifetime than high-injection data, but even this may be influenced by the majority carrier. This should always be taken into consideration when interpreting TRPL data.

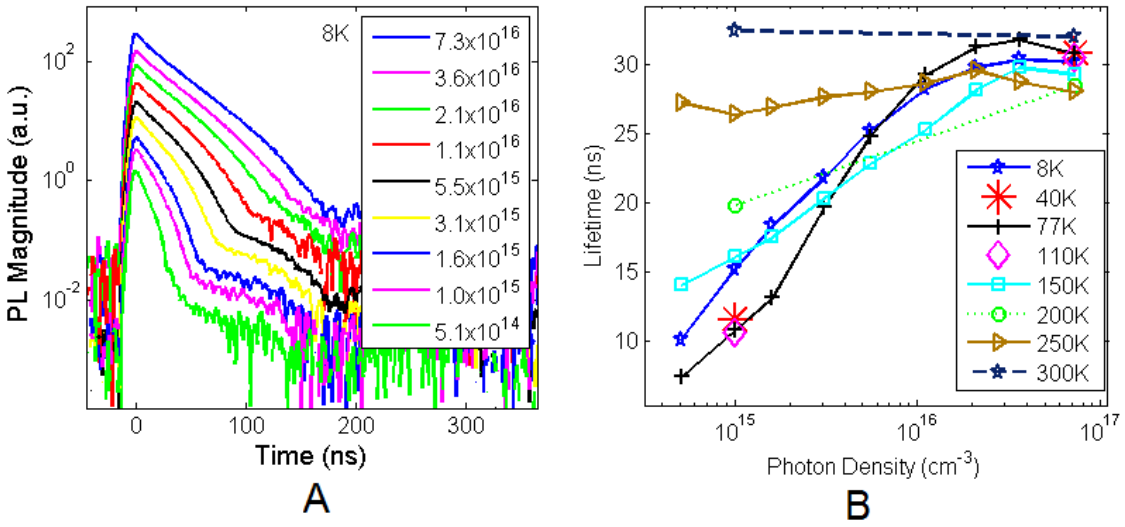

Figure 4.5: A) Example of bowing due to trap saturation. The TRPL decay is non-linear on a logarithmic plot, but rather the decay rate increases at lower injection levels. B) Lifetime as a function of injected photons, for a number of different sample temperatures.

4.3.2 Interfaces

Because of the conflicting results on the effect of interfaces on carrier lifetimes in T2SL (described in section 2.4), it seemed justifiable to investigate interfaces in this study as well. We looked strictly at the effect of different types of interfaces that can be formed during growth, to see if an optimal growth method could be determined (within the samples of this study).

Table 4.3 shows the interface growth conditions for the three samples of this study (Labeled A-C). A number of previous publications are available that document the different chemistries that form from different interface treatments [63, 64, 65, 66, 67, 68]. In this study, interfaces are referred to as Interface 1, which is above the InAs layer and below the next GaSb layer (as the sample is grown), and Interface 2 is above the GaSb layer and below the next InAs layer. Interface 1 had two different types of interface, including a 0.6 s Sb soak, where only the Sb shutter is open with the intent

Table 4.3: Measured lifetime of interface study samples at different temperatures and injection conditions: low-injection (1 to 5 x10^{15} cm^{-3}) and high-injection (7.3 x10^{16} cm^{-3}).

	Layer	A	B	C
	InAs			
	Interface 1	Uncontrolled	Sb soak	Sb soak
	GaSb			
	Interface 2	Strain comp.	Interrupt	Strain comp.
Injection	Temperature (K)		τ (ns)	
Low	8	47.1	31.5	49.4
	77	48	36.4	48.5
	300	44	42.8	47.9
High	8	36.5	30.9	37.7
	77	29.8	31.3	36.3
	300	36.5	34.8	39.2

of forming an InSb-like interface, or an "uncontrolled" interface, where no particular action was taken to force the chemistry of the interface to be InSb-like or GaAs-like. Literature [66] has shown that T2SL grown with InSb-like interfaces showed improved mobilities and reduced interface roughness compared to those with GaAs-like interfaces. Interface 2 also had two different types, an InSb strain compensation layer, where InSb is used to balance the strain caused by growing InAs layers, or a growth interrupt, where all shutters are closed with the intent of promoting an InSb-like interface [67, 68]. Sample A had an uncontrolled Interface 1 and a strain compensation layer for Interface 2; sample B had an Sb soak for Interface 1 and a growth interrupt for Interface 2; sample C had a Sb soak for Interface 1 and a strain compensation layer for Interface 2.

Because this study used identical sample architecture (figure 4.2) to that of the doping study, the representative XRD and PL plots of figure 4.3 also apply to this study. The average strain and FWHM of the dopant study also applied to samples A and C of the interface study. However, because sample B lacked an InSb strain compensation layer, the XRD results were different from A and C (which had an

average lattice mismatch of 1.2% compressive and 44 arc seconds FWHM), with a tensile lattice mismatch of -0.14% and FWHM of 50 arc seconds.

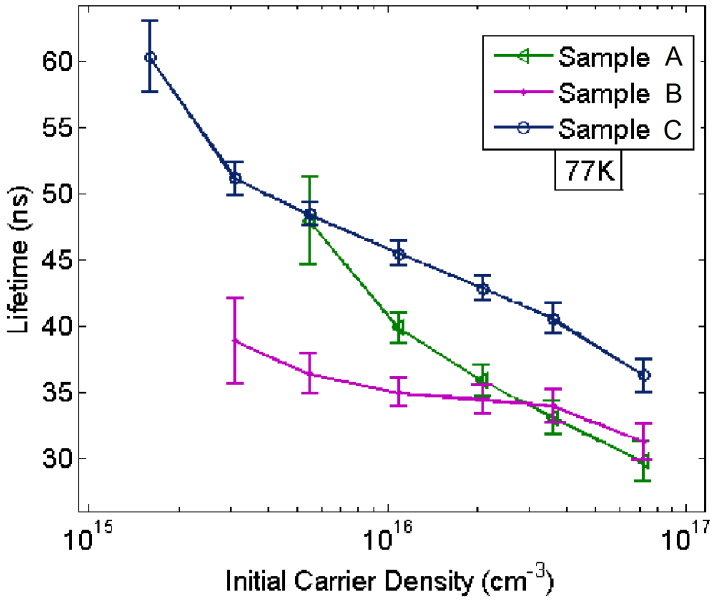

Figure 4.6: Interface study lifetimes for different initial carrier densities at 77 K.

The lifetime data revealed slight differences in carrier lifetime between samples A-C. Sample C exhibited the longest lifetimes (36-60 ns), followed by sample A (30-48 ns), and sample B had the lowest lifetimes (31-39 ns). This trend is seen in figure 4.6, which plots the lifetime of samples A-C at 77 K for different initial carrier densities. In this figure, all samples have a decreasing lifetime with increasing carrier density (which shows that trap saturation is not present in these undoped samples). Of the three samples examined, sample C's interfaces produced the longest lifetimes. Also, both of the samples with strain compensation layers (A and C) had longer lifetimes than the sample that had a growth interrupt instead (B). In fact, sample B exhibited something unusual that the other samples did not have, a fast initial decay at only 110 and 150 K (all other temperatures did not show this). This fast initial decay is shown in figure 4.7, where after the initial injection, there is a rapid decay in the 110 K and 150 K plots, followed by the slower decay, similar to the other temperatures' decay

rates, after about 5-10 ns. Because the fast decay appeared at only two temperatures, laser scattering or radiative recombination are probably not the cause, because both of these are temperature independent. Auger is also not likely, since the fast initial decay is most prominent at low injection levels, whereas Auger is most prominent at high temperatures. Therefore, the fast initial decay is attributed to a second SRH recombination trap level. Because this does not appear in the samples A or C, it is not caused by the uncontrolled interface, the Sb soak, or the InSb strain compensation layer. The unique interface in sample B is the 1-second growth interrupt, which we attribute this fast initial decay to.

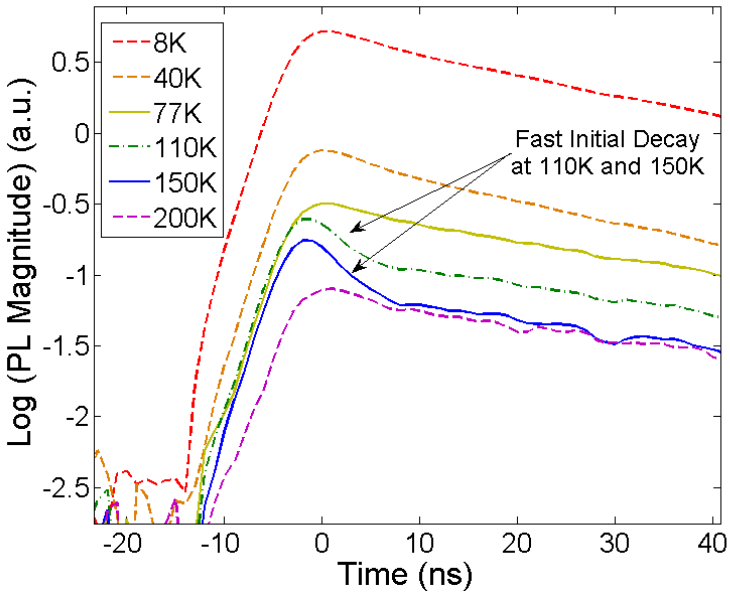

Figure 4.7: Fast initial decay at 110 and 150 K for only sample B.

4.4 TRPL summary and conclusions

Time-resolved photoluminescence was used to study the effects of doping placement and type, and interface type on carrier lifetime. Sample temperatures ranged from 8 to 300 K and initial carrier densities varied from 5.1×10^{14} to 7.3×10^{16} cm^{-3}.

For the doping study, seven samples were examined, where the doping was either only in the InAs layer, only in the GaSb layer, or in all layers for both Be and Te doping. It was found that the sample that was non-intentionally doped had the longest lifetimes (∼48 ns), Be had the second longest (10-40 ns), and Te had the shortest (∼3 ns). Also, the lifetime also followed consistent trends with which layer was doped, regardless of the doping. Placing the doping in the InAs layer produced (∼5 ns) longer lifetimes than if the doping was placed in the GaSb layer, which was, in turn, ∼5 ns longer than placing the doping in both layers.

In the interface study, three samples were grown with interfaces of either an Sb soak, a growth interrupt, an InSb strain compensation layer, or an "uncontrolled" interface. Of the three samples, the best performer had an Sb soak (interface 1)/ InSb strain compensation layer (interface 2), with lifetimes from 36-60 ns. The worst performer had an Sb soak (interface 1)/ growth interrupt (interface 2), with lifetimes from 31-39 ns, and the middle performer had an uncontrolled (interface 1) / InSb strain compensation layer (interface 2), with lifetimes of 30-48 ns. The worst performer also showed evidence of a secondary SRH trap level, presumably caused by the growth interrupt of interface 2.

While there were obviously some samples that outperformed others within this study, no radical improvements in carrier lifetime were observed. However, the results of this study do allow us to make recommendations for interfaces and doping placement and type, such as using an Sb soak for interface 1 and InSb strain compensation layer for interface 2, or using Be or non-intentional doping, rather than Te.

Chapter 5

Defect characterization of GaSb for use in InAs/GaSb Superlattices

To help understand why InAs/GaSb superlattices have such short lifetimes compared to Ga-free superlattices, the GaSb layer itself needed to be carefully studied from the perspective of its use in T2SL. While GaSb has been previously studied for defects, the effects of its use in T2SL have rarely been. Two key differences between bulk GaSb and GaSb in T2SL are: 1) bulk GaSb is grown at much higher temperatures (500°C), compared to T2SL (400-440°C), and 2) there is intermixing of the In and As from the alternate layers with the GaSb. These differences could potentially contribute to the low lifetimes found in the Ga-containing superlattices. This chapter focuses on defects in GaSb, using steady-state photocapacitance as a characterization method to show at what energy levels defects appear. First, the effect of growth temperature and In/As incorporation in GaSb is examined using photocapacitance and photoluminescence characterization techniques. Then, the use of increased cracking zone temperature of the Sb, so that the Sb monomer-to-dimer ratio is increased, is investigated as a possible method to mitigate defects.

5.1 Physics of capacitance methods for defect characterization

A metal-to-semiconductor interface or a p-n junction results in (at equilibrium) a volume ideally devoid of mobile charges, called the space charge region (SCR). On either side of the SCR, mobile charges exist, which forms a situation analogous to a parallel-plate capacitor. Thus, the diode has capacitance, which depends on the area of the diode (area parallel to the SCR), the material's dielectric constant ($\epsilon_s = \epsilon_r \epsilon_0$), the built-in ($V_{bi}$) and applied (V) voltages across the diode, and the density of ionized fixed charges in the SCR (N_{scr}) [49]:

$$C = A\sqrt{\frac{q\epsilon_s}{2}}\sqrt{\frac{N_{scr}}{V_{bi} - V}} \tag{5.1}$$

Because capacitance depends on N_{scr}, it can be utilized as a tool to characterize defect levels. Lang [69] has reviewed several capacitance-based defect characterization methods such as DLTS, admittance spectroscopy, photocapacitance, thermally-stimulated capacitance. These methods rely on an external stimulus (such as temperature, voltage pulses, or incident light wavelength) that interacts with the trap, in order to study it. A trap level can be negatively, positively, or neutrally charged, but contains either an electron or a hole at any given time. This can be used to define four processes in the trap dynamics: electron capture, electron emission, hole capture, and hole emission. Figure 5.1 illustrates these processes, for a trap at energy level E_T sitting in between the valence band at energy E_{VB} and the conduction band at energy E_{CB}.

In photocapacitance measurements, energy from incident light is used to set off emission and capture processes. This happens if the incident light is at an energy of E_T - E_{VB} or E_{CB} - E_T, which satisfies conservation of energy requirements. These emis-

sion and capture processes modify the density of ionized impurity atoms in the SCR, which changes the capacitance. By monitoring the capacitance of a sample while sweeping from higher to lower wavelengths of incident light, the emission/capture processes at specific wavelengths can be observed. Capacitance changes in photocapacitance measurements can show trap energy levels with respect to the band edges, or relative energy levels of the traps. The higher the density of that particular trap level, the more the capacitance changes. This method has been used previously for several studies [70, 71, 72].

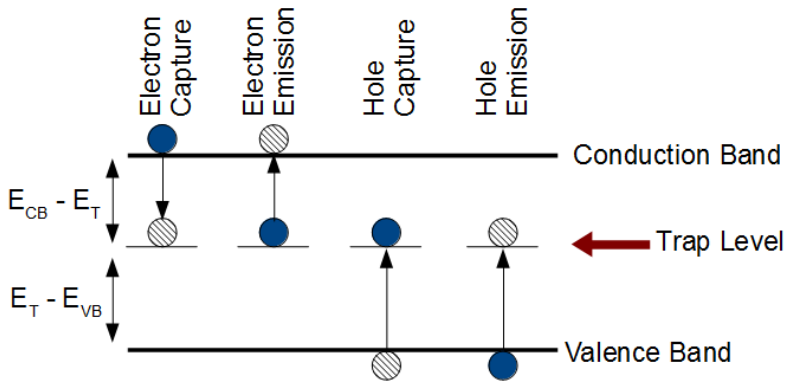

Figure 5.1: How traps interact with charge carriers: capture and emission processes. Electrons are blue and holes are hatched.

5.2 Steady-state photocapacitance setup

A diagram of the photocapacitance setup for this project is illustrated in Figure 5.2. A HawkEye IR-18 glow-bar with a maximum temperature of 1150°C and equipped with a parabolic reflector is the broad-spectrum IR source. This light gets focused onto the input slit of the monochromator (CM110 1/8-meter) by an off-axis parabolic mirror (not shown in diagram), the monochromator's internal diffraction grating is used to select an output wavelength which is then directed out of the monochromator. This light is focused by a KBr lens onto the sample under test held within the

cryostat (Janis VPF-100). The cryostat has windows made of materials such as KBr, ZnSe, KRS-5, or CaF_2 that transmit wavelengths of interest. A cryostat is useful for cryogenically cooling a sample (using liquid nitrogen or helium) under vacuum so that water vapor does not condense on the sample's surface while it is being characterized. To control the sample's temperature, a resistive heater and temperature sensor mounted near the sample, are used by a PID temperature controller (LakeShore 330) to monitor and change the temperature. A capacitance meter (Agilent 4263 LCR meter) is connected to the sample by electrical throughputs; the meter records the capacitance of the sample as the incident wavelength is varied. These values are sent to a computer via GPIB and the data is saved.

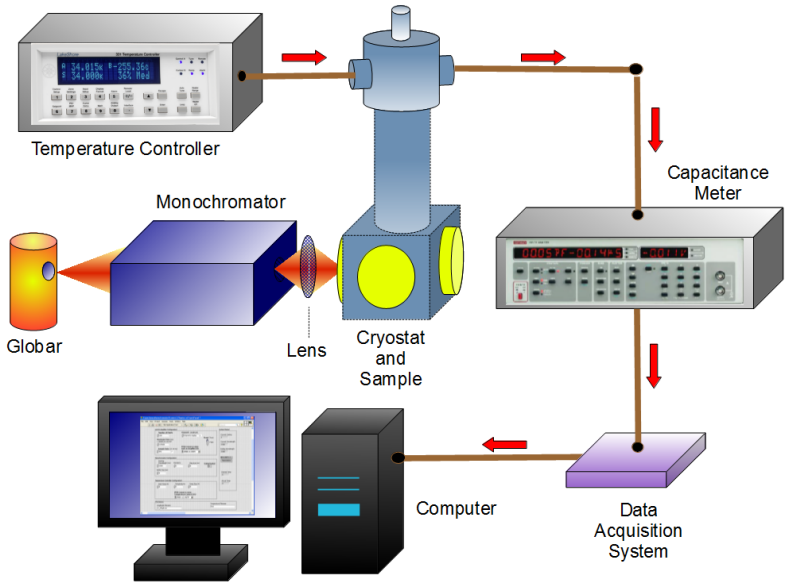

Figure 5.2: Diagram of photocapacitance setup. Light from the IR source gets focused into a monochromator with an off-axis parabolic mirror (not shown). The monochromator selects the wavelength of light to send out through the lens and to the sample in the cryostat. The cryostat is cooled using either liquid nitrogen or liquid helium and the sample temperature is controlled through resistive heating by the temperature controller. A capacitance meter measures the capacitance of the sample, and this value is recorded on a computer.

Initial versions of the photocapacitance setup did not show changes of capacitance

Table 5.1: Photocapacitance design considerations

Component	Choices	Advantage	Disadvantage	Selection
IR source	TOPAS	No monochromator	Pulsed	
	IR-18 / Monoch.	CW, non-pulsed	Reduced intensity	✓
C Measure	Lock-in Amp.	Tunable test f	Drift in data	
	Capacitance Bridge	Inexpensive, tunable f	Results delayed	
	Commercial Meter	Reliable / Immediate	Fixed test f	✓
Architecture	Schottky	No doping	Fab. challenges	✓
	Homojunction	Easy to fabricate	Doping necessary	

with variation of incident wavelength. Suspected reasons were a) too low of light intensity on the sample, b) the capacitance meter was not sensitive enough to detect changes, c) the sample was not sensitive enough to detect changes. Each of these aspects was simultaneously tackled and improved, as discussed below, with the final result being an operational setup. Design decisions made along the way are displayed in Table 5.1.

Insufficient light on the sample was suspected because the capacitance remained the same when the light was blocked from or allowed on the sample, even though it should have changed. A higher intensity, tunable IR source was needed in order for the sample to be responsive. Two viable options were an increased-intensity broad-spectrum IR source to use with the monochromator, or an optical parametric amplifier (OPA/TOPAS). As shown in Table 5.1, the TOPAS does not need a monochromator to achieve wavelength tunability, which is a big advantage since a monochromator attenuates most of the light intensity. However, a major disadvantage is that the TOPAS intensity out is pulsed as a function of time, so that the capacitance varies for a constant incident wavelength. In contrast, the IR-18 and monochromator combination has intensity attenuation, but also provides a continuous, non-pulsed light source. Therefore, the IR-18 and monochromator combination were selected for this setup, instead of the TOPAS.

Several different capacitance measurement schemes were attempted and evaluated

for this project. Important aspects in choosing a capacitance measurement method were the ability to vary test frequency, apply a voltage bias, ease of data collection, measurement accuracy, capacitance range, and system price. A lock-in amplifier was connected to a circuit to measure changes in capacitance. While it was capable of measuring capacitance values, and the test frequency could be tuned over a wide range, but the circuit tended to drift over time, which introduced unwanted noise (variation of several pF). A capacitance bridge circuit had similar advantages and disadvantages as the lock-in amplifier setup, with tunable test frequencies and suffered from drift over time. This drift was what led us to favor the commercial capacitance meter, which was reliable, had little time variation for a fixed capacitance, and also provided an immediate value in capacitance, rather than having to calculate it from a linear relationship of output voltages vs. capacitance. One major disadvantage of the commercial capacitance meter that we could afford was there were a limited number of available test frequencies.

Finally, the device structure had to be considered. From the description in Section 5.1, in order to perform a photocapacitance measurement, the sample has to have a space-charge region, either from a Schottky metal contact or by forming a homojunction through doping. The major problem with using a homojunction is that the doping atoms used to form the space-charge region could potentially appear in the resulting photocapacitance data, which is not a problem for the Schottky diodes that use a metal-insulator-semiconductor interface to form the space-charge region. Yet, producing a high-quality Schottky diode for such narrow-bandgap materials is challenging, whereas for the homojunction this was not expected to be an issue. Because the homojunction had to be doped, which had the potential to impact the results, it was not used in this study.

The design of both the Schottky diode had to account for the theoretically-predicted depletion widths as well as processing constraints. In theory, the depletion

region width created by a metal-semiconductor junction is [73]:

$$W = \sqrt{\frac{2\epsilon_s(V_{bi} + V_r)}{eN_a}} \tag{5.2}$$

Figure 5.3 shows the calculated depletion widths for different metals on p-type GaSb. The values were used to design the thicknesses of GaSb Schottky diode structures. Figure 5.4a illustrates the metal-semiconductor structure.

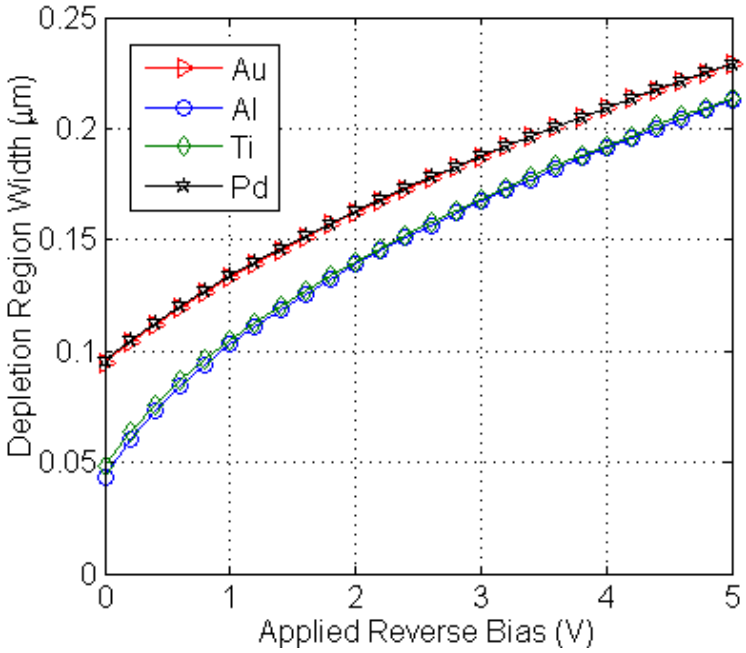

Figure 5.3: Calculated values of Schottky diode depletion width for different metals on GaSb.

In practice it is difficult to predict real depletion widths and what metals will make the best Schottky diodes. Literature has shown barrier heights of 0.65 eV for Al, 0.6 eV for Au, and 0.5 eV for Ni [74], for example, on n-type GaSb. Because Schottky barriers can be difficult to fabricate, especially for narrow-gap semiconductors, a metal-insulator-semiconductor structure was also considered. A thin layer of oxide (see figure 5.4b) produces a more ideal Schottky diode [75]. Before applying the oxide, the samples were dipped in a solution of HCl : H_2O (1: 5) for 30 seconds, to remove

native oxides. Then, to make the oxide layer, 40 to 50 Å of SiO_2 was deposited using electron-beam evaporation of SiO_2 pellets in a vacuum chamber.

A diagram of a metal-insulator-semiconductor (MIS) is shown in figure 5.4c. The top metal layer is where the voltage bias is applied, which rests on top of a insulator layer of thickness d with fixed capacitance C_i, which is then on top of the semiconductor layer with variable capacitance C_d [7]. A thinner oxide layer allows for tunneling; too thick of a layer will act as a barrier. Therefore, 30 Å is the recommended thickness [75].

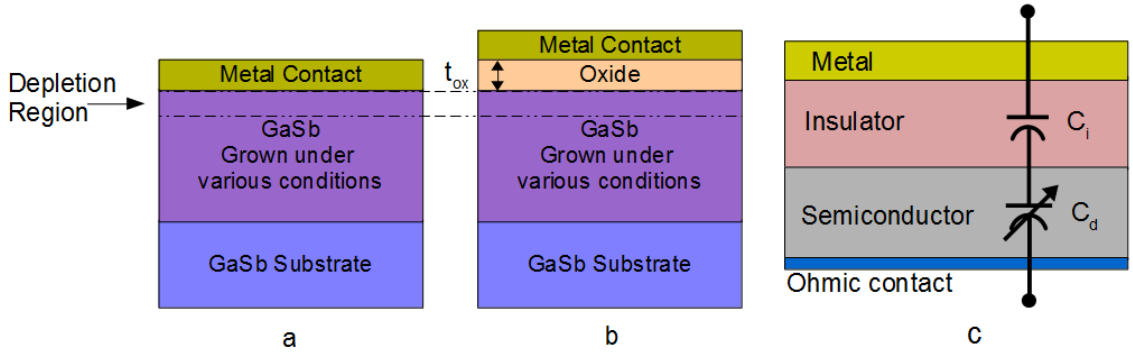

Figure 5.4: Schottky diode structures. a) Semiconductor-metal junction, b) metal-insulator-semiconductor junction, c) MIS equivalent circuit.

5.3 Photocapacitance sample preparation

Since photocapacitance measurements are performed on fabricated devices at cryogenic temperatures, there are a number of steps the samples go through before these measurements can be made. After the samples are grown in a molecular beam epitaxy system (described in section 3.1), they were fabricated into single-pixel device structures, either with the Schottky or homojunction diode mask set (described in section 3.2). These samples were then cleaved into individual dies, and glued onto 68-pin chip carriers with silver epoxy. Next, the epoxy was cured and the individual test pixels were wire bonded to the chip carrier's electrical leads. Finally, current-

voltage characteristics were collected for each sample, to both evaluate the quality of rectification of each diode, as well as to determine which were the best devices to characterize with photocapacitance.

5.4 Photocapacitance measurements

Each photocapacitance data set was taken using the same method. First, the sample was cooled in the cryostat to the desired temperature and allowed to stabilize for a minimum of half an hour. Then, the sample was connected to the capacitance meter by a 4-point probe configuration. Light from the IR source and monochromator combination was directed onto the sample, and the sample was carefully positioned by a 3-dimensional linear translation stage to maximize the change in capacitance between when light was allowed on it and when light was blocked.

To condition the sample prior to every run, any hole traps were filled by briefly shining above-bandgap light on the sample. Then, the photocapacitance data was collected, starting with the lowest energy (highest wavelength) and scanning to the highest energy (lowest wavelength) of interest, while the capacitance of the sample was monitored. At each wavelength, the sample was allowed a settling time before capacitance data was collected. The capacitance data from each wavelength was measured by collecting several data points and averaging.

There are several variables that can be tuned in a photocapacitance measurement, including bias voltage, AC capacitance measurement frequency, AC measurement voltage, sample temperature, and monochromator slit size. Each of these (see figure 5.5) was examined before the majority of the sample measurements were performed. This allowed for guidelines to be defined for test conditions, for optimal ranges of these variables.

Following figure 5.5, the AC test voltage of the capacitance meter was varied from

0.02 to 1.0 V, and the best defect resolution was obtained around 0.4 V. Near the extremes tested, the signal to noise ratio reduces and it is more difficult to discern changes in capacitance. Varying the AC test frequency of the capacitance meter from 100 Hz to 100 kHz also showed an optimal range. The low test frequencies (100 and 120 Hz) produced noisy signals, while the 1, 10, 20 and 100 kHz had strong signals with clearly defined capacitance changes. DC bias appeared to have little effect on the sample, though a stronger signal-to-noise ratio might be expected with increasing negative bias, because the space-charge region would become wider, allowing for a larger volume of the sample that could react to the incoming photons. Sample temperature had a major impact on the results. A jump from 80 K to 150 K obscures most features. This may indicate that going to even lower temperatures would aid in producing more meaningful data. Notice that there are jumps in the sample temperature plot. This is due to bad connections, which were fixed in later measurements. Finally, the monochromator slit size data shows that there is a trade-off between wavelength resolution and signal-to-noise ratio. For this particular sample slit size of 0.6 mm provided enough light to have good signal-to-noise, but with enough resolution to see less prominent details in the photocapacitance plot. Selection in slit size depends strongly on the sample response to light.

For all of the photocapacitance experiments (unless otherwise noted) the following conditions were used: a AC test frequency of 10 kHz, a AC test voltage of 0.4 V, a sample temperature of 77 K. The DC bias and monochromator slit size varied too much to generalize.

5.5 Photocapacitance results

Table 5.2 displays all of the samples characterized with the photocapacitance technique. Chapter 2 discussed possible causes of low lifetimes in T2SL; the remainder of

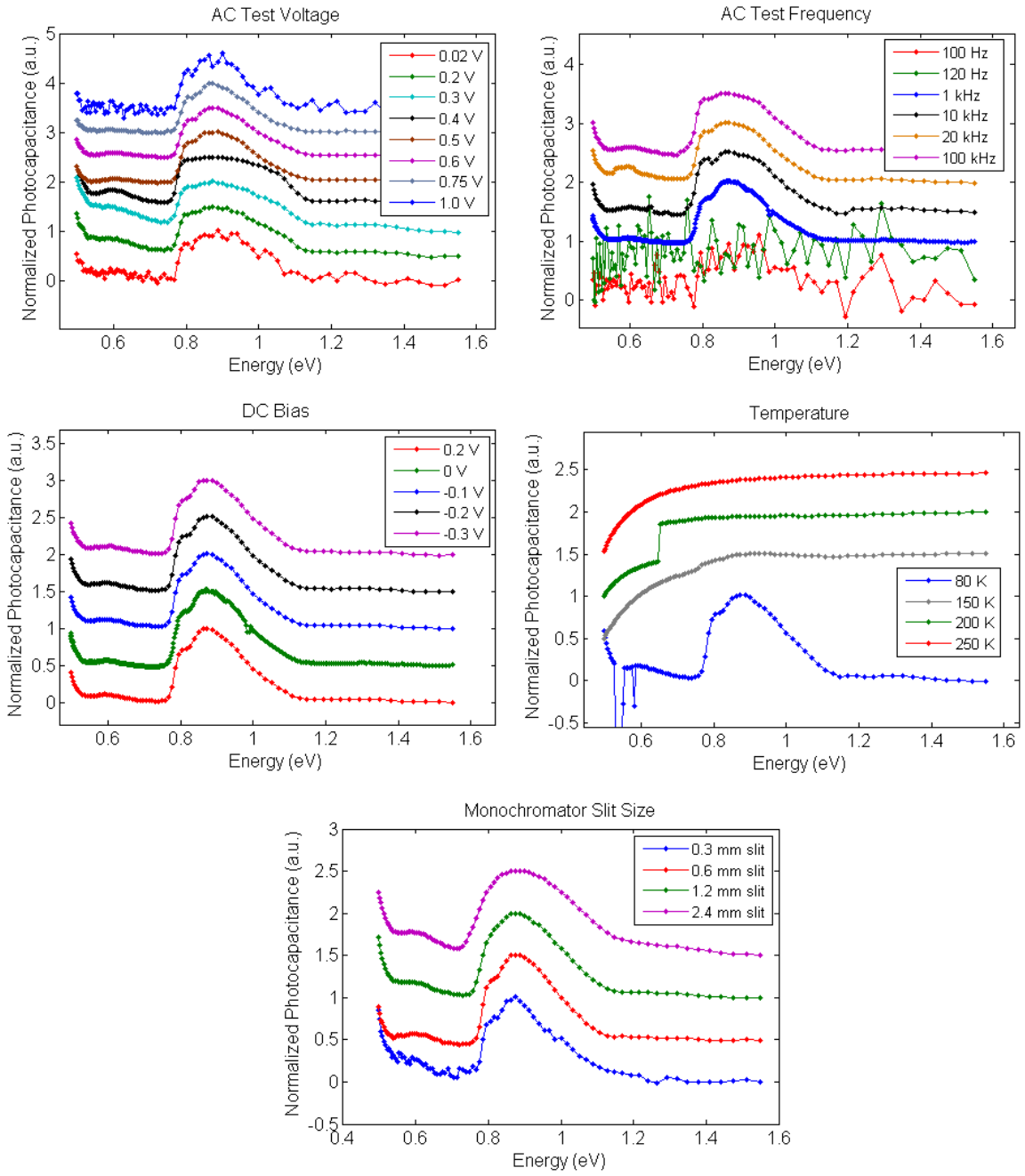

Figure 5.5: Tested photocapacitance variables: AC test voltage, AC test frequency, DC bias, sample temperature, and the slit size of the monochromator. This test helped determine what effects these different parameters would have on the measurement, and provided guidelines for test conditions.

Table 5.2: List of samples characterized by photocapacitance, dark current, and photoluminescence. Samples 8 and 9 had a n-i-p architecture.

#	Sample	T_{grow} (°C)	Sb Cracker (°C)
1	GaSb	400	900
2	GaSb : In	400	900
3	GaSb : As	400	900
4	GaSb	500	900
5	GaSb	400	1100
6	8/8 T2SL	400	900
7	8/8 T2SL	400	1100
8	nip 10/10 T2SL	400	900
9	nip 10/10 T2SL	400	1100

this chapter focuses on relating defect levels identified by photocapacitance to specific causes from growth conditions. Three different conditions are explored: 1) effect of In and As incorporation in GaSb, 2) effect of growth temperature on GaSb, 3) effect of growing with Sb_1 vs. Sb_2 on GaSb and T2SL.

5.5.1 Incorporation study

Samples 1-3 in table 5.2 were grown to see if any defects, observable through photocapacitance measurements, were formed in GaSb through doping by In and As. Since these atoms constitute the layers above and below each GaSb layer, they are very likely to mix into the GaSb. Each of these samples was grown on undoped (residually p-type) GaSb epi-ready, double-side polished (100)-oriented substrates, at the T2SL growth temperature (∼400°C). The epitaxy was approximately 4 μm-thick for all three devices, and was designed to be fabricated into Schottky diodes (see section 3.2). Sample 1 was an undoped GaSb control, sample 2 was GaSb incorporated with 1.2% In (or $In_{0.012}Ga_{0.988}Sb$), and sample 3 was incorporated with 2.2% As by opening the valve to 200 mils but growing with the As shutter closed.

Incorporation levels were confirmed by overlaying the x-ray diffraction (XRD) data from each sample with simulated XRD from RADS Mercury simulation soft-

ware, to reconstruct the concentration of In and As in the ternary ($GaAs_{0.022}Sb_{0.978}$ and $Ga_{0.988}In_{0.012}Sb$) epitaxy based on substrate-to-epitaxy lattice constant mismatch. An example is shown in figure 5.6. Nomarski interference microscopy was also used for post-growth characterization. This revealed a relatively defect-free surface for sample 1 and cross-hatching for samples 2 and 3. This cross-hatching indicates that this ternary growth on GaSb was beyond the critical thickness, which is the maximum thickness an epitaxial layer of one lattice constant can be, when grown on a crystal of different lattice constant before excessive strain causes defects to form (see section 3.1). Using equation 3.3, the critical thickness for the epitaxy of sample 2 (In-incorporated) was ∼400 nm and ∼190 nm for sample 3 (As-incorporated).

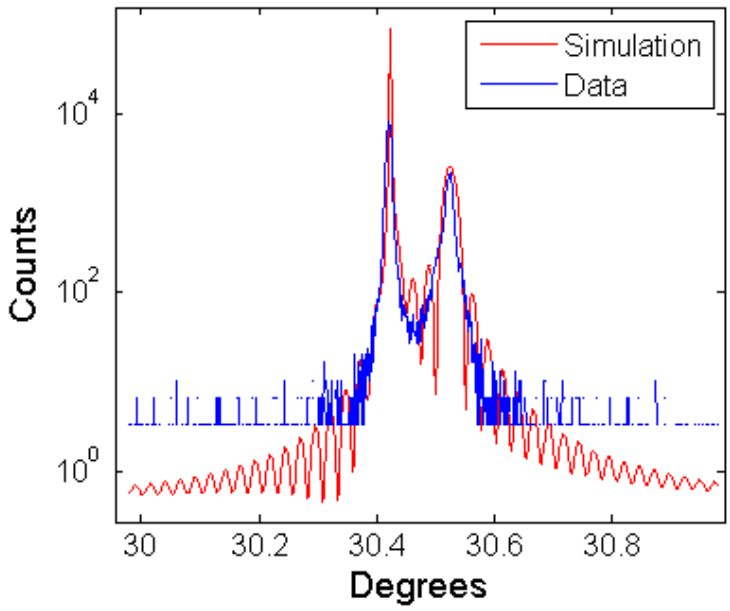

Figure 5.6: X-ray diffraction plot and simulation overlay for the $Ga_{0.978}As_{0.022}Sb$ sample. By varying the % composition of the As in the simulation, the simulation was matched to the measured XRD plot, allowing determination of the composition.

Photoluminescence plots of these three samples are given in figure 5.7. The addition of In actually increased the PL intensity compared to the control sample, while As reduced it. The control sample's intensity was 80% of the GaInSb sample's, and

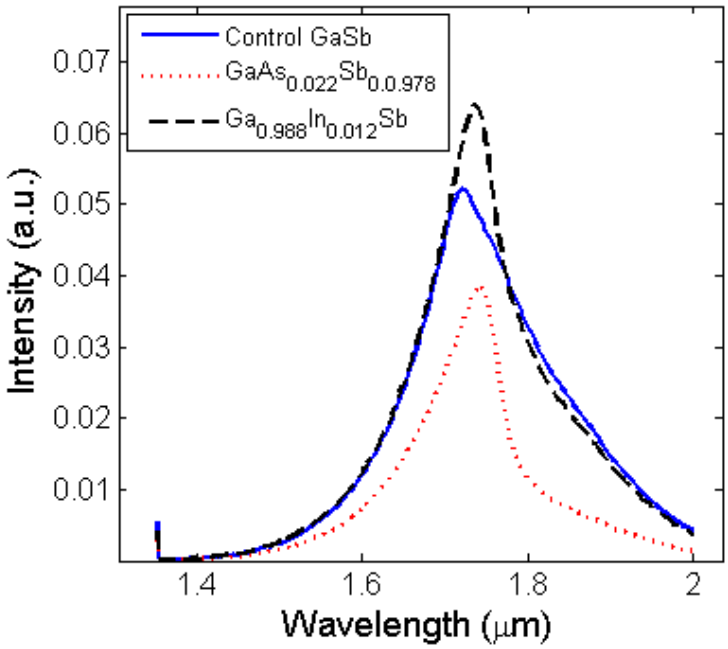

Figure 5.7: Photoluminescence of the incorporation samples at room temperature.

the GaAsSb sample's intensity was 60% of the GaInSb sample's. The stronger PL of the In-incorporated sample is expected; a previous study [48] had shown increasing lifetime in InAs/$In_xGa_{1-x}Sb$ superlattices with increasing In content. The reduced PL intensity of the GaAsSb sample may support why growers promote InSb-like interfaces rather than GaAs-like ones. Degrading PL intensity may coincide with reduced sample performance for T2SL grown with GaAs-like interfaces.

These samples were then fabricated into Schottky diodes, wire bonded, and characterized with steady-state photocapacitance. Initial wavelength scans at 77 K starting from 7 μm and ending at 0.8 μm (with the monochromator equipped with a grating optimized for 2.5 to 9 μm) revealed a number of rises and falls in capacitance, shown in Figure 5.8. To delineate which features were actually at the correct wavelengths and which were artifacts of the monochromator, two long-pass filters, one that passed wavelengths above 2500 nm (energy below ~0.5 eV) and one that passed wavelengths above 800 nm (energy below 1.55 eV), were used. The 2500 nm filter showed a pho-

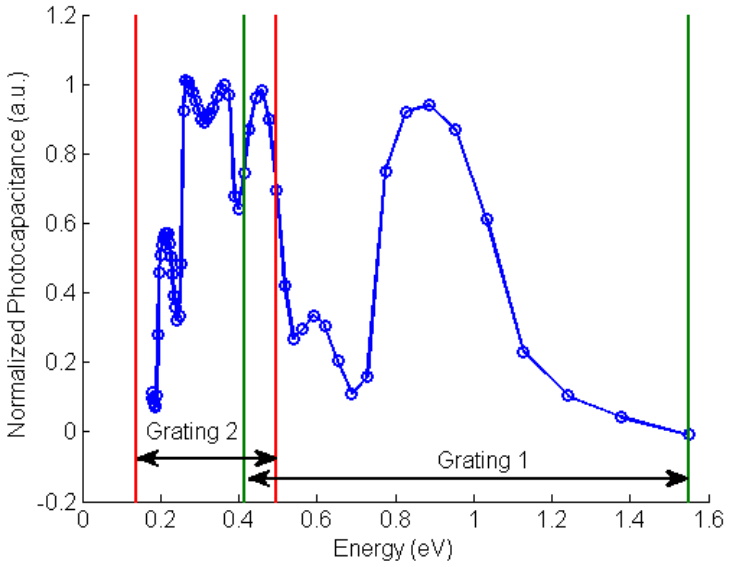

Figure 5.8: Capacitance variation for different incident wavelengths. The optimal ranges for the available gratings are shown. Grating 2 was used to collect this particular spectrum.

tocapacitance plot with no changes in capacitance, while the 800 nm showed all of the features from figure 5.8. Therefore, all of the features above 2500 nm are most likely due to higher-order diffraction of the light from the 800 - 2500 nm range. The photocapacitance for Samples 1-3 is thus plotted in figure 5.9, for the range where higher-order diffraction did not play a role. This measurement was performed with a 0.6 mm monochromator slit size, and zero voltage bias.

Two features appear in the photocapacitance plots for all of the samples, labeled as features A and B. Feature A begins at approximately 0.5 eV with a maximum at about 0.6 eV and feature B is at approximately 0.8 eV. Because the bandgap of GaSb is calculated to be 0.8 eV at 77K [76], feature B can be attributed to transitions from traps slightly above the valence band edge to the conduction band. Feature A is near mid-gap, and appears regardless of whether the material is pure GaSb, or alloyed with In or As, suggesting that it is intrinsic to GaSb. These results appear to confirm the presence of a GaSb trap feature at 0.63eV first reported by Kuramochi [77]. They

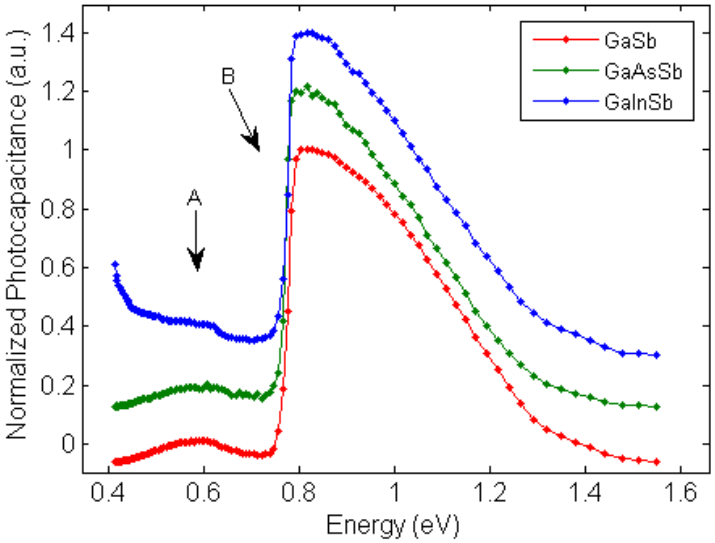

Figure 5.9: Corrected photocapacitance spectrum in which higher-order diffraction effects from the monochromator are discounted. Data is stacked for easier comparison.

had attributed this trap to Te diffused into the GaSb from the Te-doped substrate. Te is likely not the cause of this level in the photocapacitance results, since Te was not intentionally put into the structure and the substrates were undoped. However, it could still be present in the background levels of the growth chamber and cannot be completely ruled out. The change in capacitance of feature A is smaller for the sample with In incorporation. This may indicate a reduction in the trap density for this sample.

5.5.2 GaSb growth temperature study

Because Svensson [40] had such a convincing argument that the low lifetimes in T2SL were due to growing GaSb at low temperatures, we wanted to find out if any change in defect levels could be detected through photocapacitance measurements. For the growth temperature study, a GaSb sample (sample 1) grown at T2SL growth temperature (∼400°C) and one at 500°C (optimal GaSb growth temperature, sample 4) were fabricated into Schottky diodes and their photocapacitance spectra were

measured with 2.4 mm monochromator slits and a 1 V applied reverse bias. The results are shown in figure 5.10, which shows that the peak normally observed at 0.5 eV for the samples grown at T2SL temperature is much smaller in sample 4. This plot looks very similar to the GaInSb photocapacitance result in figure 5.9.

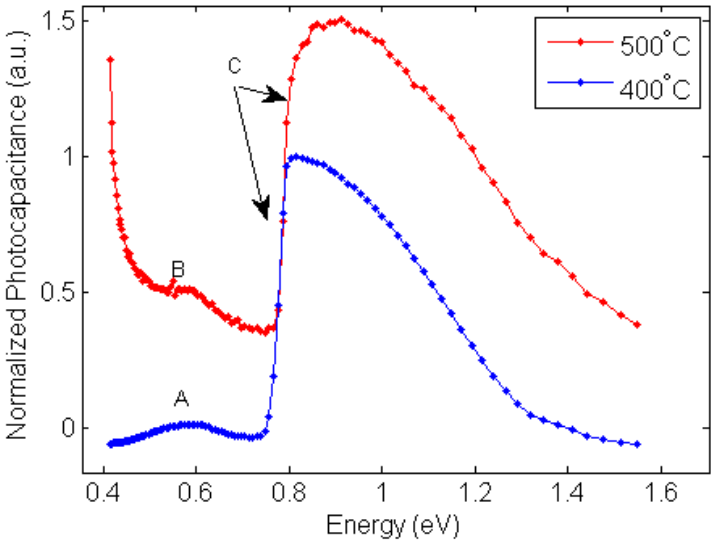

Figure 5.10: Photocapacitance spectrum comparison for GaSb grown at 400°C and 500°C. These plots are stacked for easier comparison.

The reduced change in capacitance of this feature may suggest that the trap level seen in sample 1 has changed for sample 4. However, there is still a feature present, even for the sample with increased the growth temperature. Future work for this study will require several samples grown over the range between 400 to 500°C, to document more gradual changes in the photocapacitance results. Lower-temperature measurements could be useful in clearer observations of the changing capacitance of this trap feature.

Photoluminescence measurements were conducted on these samples as well, with room-temperature results plotted in figure 5.11. The GaSb grown at 500°C does have a slightly higher intensity, 1.3 times that of the sample grown at ∼400°C. This suggests that there might be a slight improvement in GaSb quality with higher temperatures,

though this difference is small enough that it could be within the variation of the PL intensity across the sample.

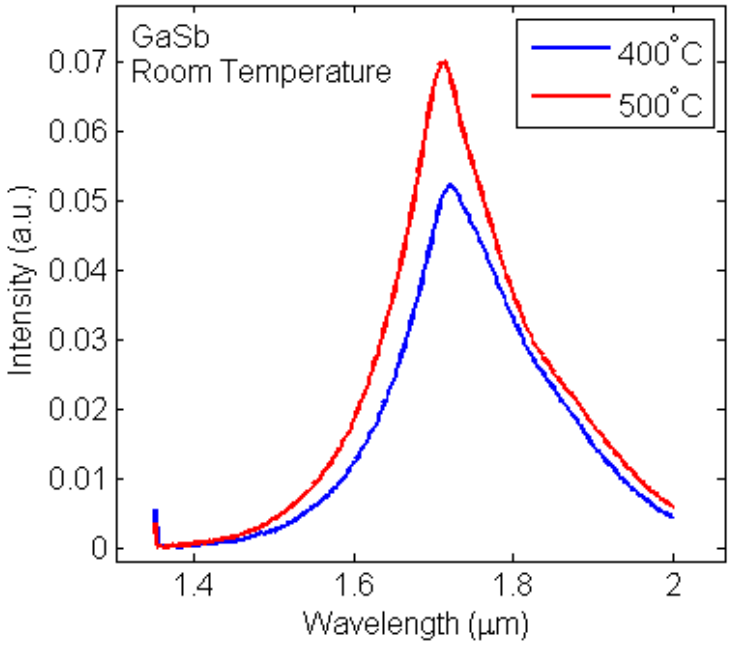

Figure 5.11: Room-temperature photoluminescence comparison for GaSb grown at 400°C and 500°C.

5.5.3 Comparison of GaSb grown with Sb_1 vs. Sb_2

Literature [40] has shown that the substrate temperature required to grow T2SL is sub-optimal for growing GaSb because the carrier lifetimes in the GaSb are reduced. Bulk GaSb is typically grown at ~500°C, whereas T2SL is grown about 100°C colder. Since the growth temperature cannot be raised without destroying the superlattice, the best approach is to find ways to grow high-quality GaSb at T2SL growth temperatures.

One solution may be to use Sb monomers (Sb_1) rather than dimers (Sb_2). An order of magnitude photoluminescence intensity improvement of GaSb grown with Sb_1 instead of Sb_2 has been previously reported on by Xie [78]. A separate study

by Brewer [79] found that Sb_1 more readily bonded to defect sites, thus reducing the number of active defects and lowering the residual p-type nature of GaSb by half.

The goal for this experiment is to try using majority Sb_1 for growing GaSb at T2SL growth temperatures, to see if there are any performance improvements in the T2SL. This was approached from two angles 1) characterize the defect levels for GaSb grown with Sb_1 and Sb_2, and 2) characterize and compare the dark current for SLS structures grown with higer Sb_1 to Sb_2 ratios. Initially, Sb is sublimated in the base of the source as Sb_4. The end of the source, near the shutter is heated enough to crack the Sb_4 into Sb_2 and Sb_1. By increasing the cracking zone from our typical 900°C to 1000°C or 1100°C, we increase the ratio of Sb_1 to Sb_2. The structures for each of these tests is shown in figure 5.12; a) shows a 10/10 T2SL-based n-i-p diode that was used to characterize dark current, b) shows bulk 8/8 T2SL design to be characterized by the photocapacitance setup.

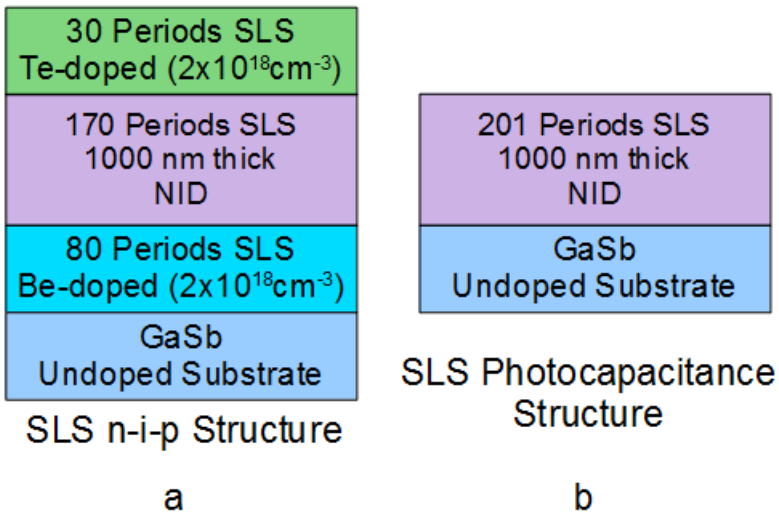

Figure 5.12: Structures grown for studying the effects of growing with majority Sb_1 compared to Sb_2. Structure (a) is composed of 10/10 T2SL, while structure (b) is composed of 8/8 T2SL.

Prior to growing these structures, Sb fluxes were optimized for increased Sb_1/Sb_2 ratio to produce low surface defect counts visible using Nomarski interference mi-

Table 5.3: Sb valve setting (Sb/Ga flux ratio) optimization for GaSb samples grown with the Sb cracker at 1000°C.

Sample	Valve Opening	Defect pixel count
1	50 mil	0.056
2	64 mil	0.009
3	81 mil	0.1

croscopy. It is important to note that increasing the cracker temperature significantly reduced (by a factor of 4) the number of defects visible by Nomarski. Also, this reduction was repeatable on both our V80 and Gen10 MBE systems. Table 5.3 displays the samples grown with various Sb valve settings and the resultant defect percentage. This defect count was determined using in-house image processing software (see figure 5.13) that removes the background intensity variation from the Nomarski image, increases the contrast, and utilizes a user-defined threshold level to mark pixels as defects. The defect pixels were then counted and divided by the number of non-defective pixels, to get the defect pixel count. It was found that an Sb valve setting of 64 mil produced the lowest defect counts. This valve setting was used for the next experiments.

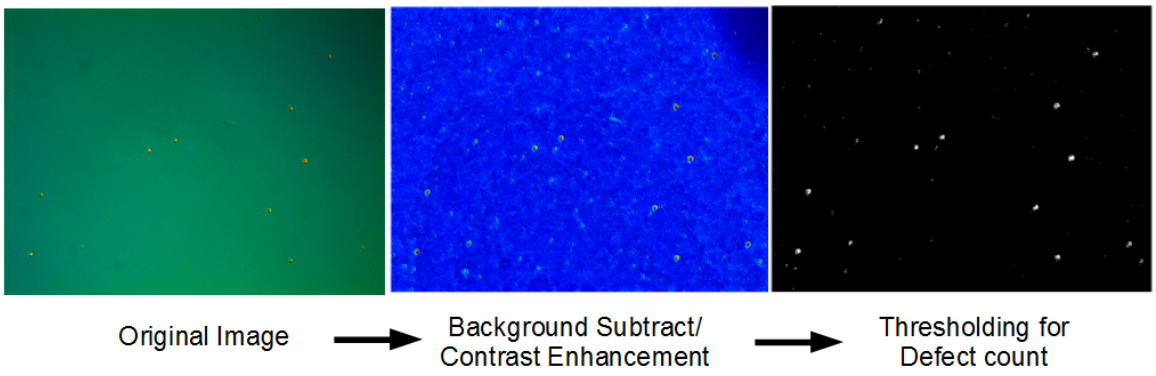

Figure 5.13: Image processing to perform defect count on Nomarski images.

From table 5.2, the n-i-p samples, sample 8 (900°C Sb cracking zone) and sample 9 (1100°C Sb cracking zone), and the bulk 8/8 T2SL samples (sample 6 (900°C Sb cracking zone) and sample 7 (1100°C Sb cracking zone) were grown.

After growth, photoluminescence spectroscopy was performed to compare samples 6 and 7, as shown in figure 5.14. The PL intensity of the sample 7 with higher cracker temperature, has approximately twice the PL intensity of sample 6. This may indicate a reduced SRH recombination and increased radiative recombination.

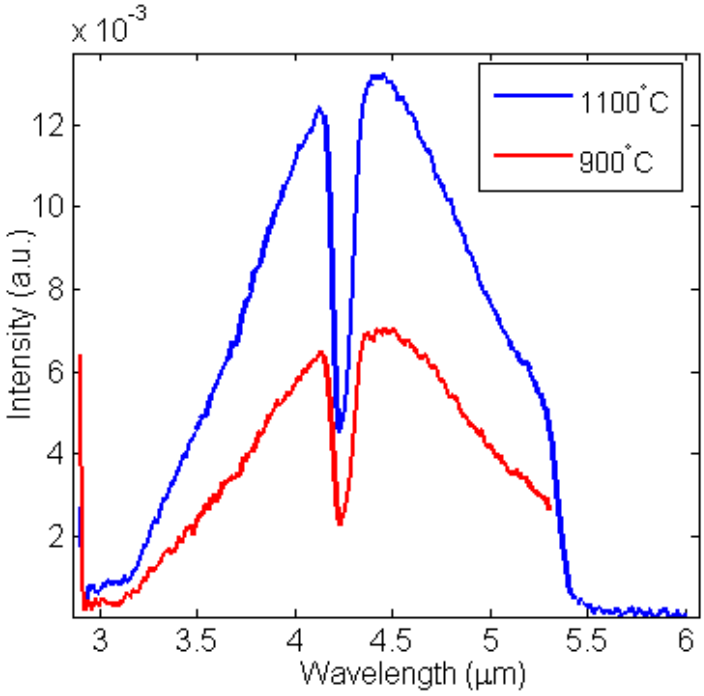

Figure 5.14: PL intensity comparison between samples 8 ML InAs / 8 ML GaSb T2SL samples grown with different Sb cracker temperatures.

The n-i-p samples were then processed into single-pixel device structures, using a plasma etch, SiN_x passivation, and Ti/Pt/Au contacts. Next, the samples were attached to chip carriers and wire bonded, to make electrical contacts to various devices. Temperature-dependent dark current measurements were performed in a close-cycle cryostat, with an available temperature range of ∼15 K to above room temperature. A cold shield was placed around the sample to minimize the noise from the surrounding environment. The dark current of the sample 9 (higher Sb_1) was found to be ∼1-2 orders of magnitude higher than the dark current of sample 8 (lower Sb_1), as shown in figure 5.15, for four different devices on each sample. We

attribute this dark current to the Sb source needing more outgassing and at higher temperatures than we had used initially. Because of the lower surface defect counts and improved PL intensity, we are not yet ready to rule-out this method as a potential way to improve T2SL performance.

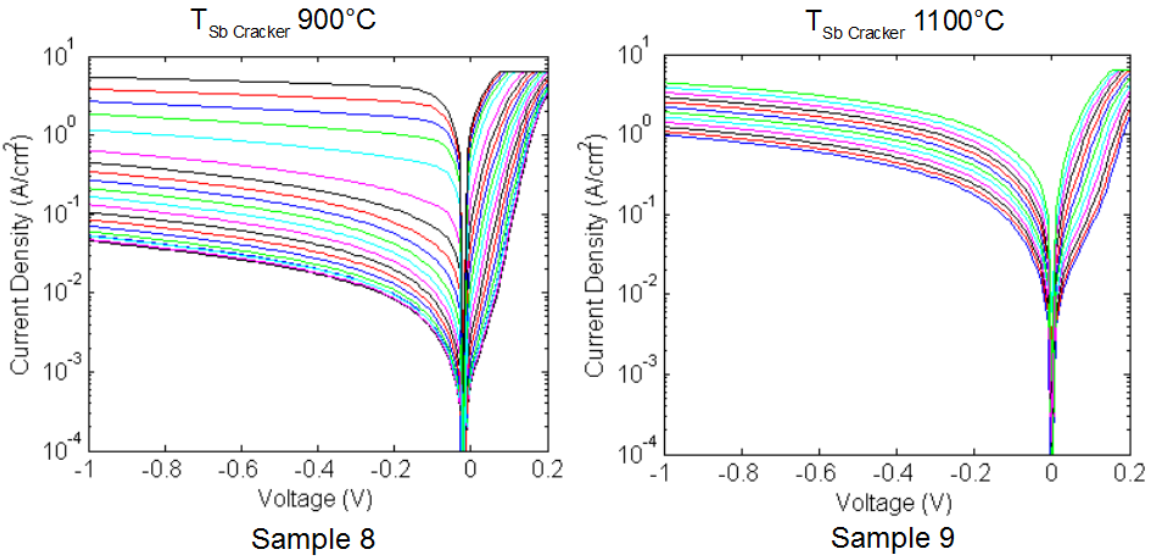

Figure 5.15: Dark current density comparison for samples 8 and 9 from 90 K to 300 K.

5.6 GaSb defect study conclusions

The defects of GaSb, specifically those likely to be in the GaSb layers of T2SL were studied. First, the effect of adding 1.2% In and 2.2% As to GaSb was investigated. PL measurements indicated that adding In slightly increased the PL intensity, while As decreased it, relative to the control sample. Photocapacitance results showed two main features, a capacitance change (Feature B) at 0.8 eV, which was attributed to traps near the conduction and valence bands, and a capacitance change (Feature A) at about 0.5 eV, attributed to trap levels close to the middle of the bandgap. The GaInSb sample had a smaller change in magnitude for its Feature A, and this sample had the brightest photoluminescence intensity of the three samples. This result could

be compared to a lifetime study that had shown an increase in InAs/$Ga_xIn_{1-x}Sb$ superlattice lifetimes with higher In concentrations. This mitigation of traps from In incorporation might be observed in this photocapacitance study.

Photocapacitance was also used to compare bulk GaSb samples, one grown at the preferred GaSb growth temperature of 500°C and the other at ∼400°C. Similar to the GaInSb sample, the sample grown at a higher temperature had a less pronounced change in capacitance for the 0.5 eV feature, once again possibly indicating a reduction in the trap density. The higher temperature sample also had slightly higher PL intensity than the lower temperature sample. This observation supports the idea that the low growth temperatures of T2SL promotes defect formation in the GaSb layers.

Growth of GaSb and T2SL with higher Sb cracker temperatures was also researched. The motivation was that increased cracking zone temperature would produce more Sb monomers, which have been previously reported to improve photoluminescence intensity and reduce the residual p-type background of GaSb [79, 78]. The residual p-type background is thought to be due to the Ga-vacancy and Ga on Sb antisite complex ($V_{Ga}Ga_{Sb}$) [51]. Growing with increased Sb monomoers was pursued as a possible strategy for growing GaSb at the lower temperatures required for T2SL. Growing GaSb with the higher Sb cracking zone temperature (1000 - 1100°C) produced samples with far fewer surface defects visible with a Nomarski microscope, and the 8/8 T2SL sample grown with this recipe had double the photoluminescence intensity compared to that grown with the typically used cracking temperature (900°C). However, the n-i-p devices grown with a 1100°C Sb cracking temperature had higher dark current than those grown with the 900°C cracking temperature. So, although the photoluminescence intensity and Nomarski images show improvements for GaSb with higher Sb cracking temperatures, the dark current is actually worse. Future work would be to try this growth in a different MBE system, to see if this is a universal

problem, or merely an issue with this particular Sb source.

Chapter 6

Conclusions and Future Work

InAs/GaSb type-II strained layer superlattices suffer from reduced minority carrier lifetimes, resulting from trap levels that cause Schockley-Read-Hall recombination. These low lifetimes lead to reduced signal-to-noise ratio and higher dark current. Therefore, increasing the lifetime is important for improving this material's performance. However, to increase the carrier lifetimes, the origin of the traps must first be understood. The traps could come from several places, including the interfaces between the InAs and GaSb layers, the intermixing between these layers, or the constituent materials themselves.

Temperature-dependent time-resolved photoluminescence was used to determine the effect on the carrier lifetime of the InAs and GaSb interfaces formed using different growth parameters (such as Sb soak, growth interrupt, InSb strain compensation layer, or no deliberate interface). Three samples were grown for this study. It was found that using an Sb soak between the InAs and GaSb growth sequence and an InSb strain compensation layer between the GaSb and InAs growth sequence produced the longest lifetimes of the samples examined, with lifetimes of 36-60 ns, as compared to the lowest performer (Sb soak between the InAs and GaSb, and growth interrupt between the GaSb and InAs) with lifetimes of 31-39 ns. The third, middle-performer

sample had lifetimes of 30-48 ns and had no deliberate interface between the InAs and GaSb, and an InSb strain compensation layer between the GaSb and InAs. The worst performer also showed evidence of a secondary trap level caused by the growth interrupt. Although modifying the interface did cause differences in lifetimes between samples, no observation in dramatic improvement in lifetime was observed. The results of this study do point to an optimal choice within the scope of this work, but the root cause of the low lifetimes is not removed from these samples by modifying the interfaces.

Temperature-dependent time-resolved photoluminescence was also used to see the effect of doping atom placement and type on carrier lifetime. Two types of doping atoms, either Te or Be, were placed in either the InAs layer, the GaSb layer, or both layers, and the lifetimes were compared. The control sample exhibited the highest lifetimes (48 ns), while doping with Be reduced the lifetime to 10-40 ns, and doping with Te lowered the lifetime below 3 ns, the minimum resolvable time of the measurement system. As for the placement of the doping atom, regardless of the doping type, doping the InAs layer allowed for $\sim$5 ns longer lifetimes than doping the GaSb layer, and doping the GaSb layer, in turn, produced lifetimes $\sim$5 ns longer than doping both the InAs and GaSb layers.

The GaSb layer in the InAs/GaSb superlattices was targeted as a source the recombination centers. Bulk GaSb was grown under various conditions and defects were characterized using photocapacitance spectroscopy. To learn how mixing between the InAs and GaSb impacts the GaSb, bulk GaSb, $Ga_{0.988}In_{0.012}Sb$, and $GaAs_{0.022}Sb_{0.978}$ were grown at T2SL typical growth temperatures, processed, and characterized with photocapacitance at 77 K. The photocapacitance plots revealed a capacitance change starting at 0.5 eV in each sample. At this temperature, GaSb has a bandgap of 0.8 eV, and the trap level is about 0.1 eV from midgap. The capacitance change was reduced in the sample incorporated with In, compared to the control and the sample

with As incorporation. This observation suggests a possible improvement when In is added, and this is supported by previous observations that adding In to the GaSb layer in T2SL increases the carrier lifetime.

Next, the effect of growth temperature on traps was examined. Two bulk GaSb samples were grown, one at about 500°C (typical GaSb growth temperature), and the other at the typical T2SL growth temperature, which was 25°C less than the RHEED transition temperature (or approximately 400°C). A comparison of these samples' photocapacitance plots showed that the mid-gap trap seen in the incorporation study at 0.5 eV was not as pronounced in the sample with the higher growth temperature. This suggests that the trap level is mitigated, but not completely removed when the GaSb growth temperature is increased. Future investigations are needed to characterize GaSb samples grown at different temperature steps, to see the variation of the trap levels with temperature.

Finally, the effect of growing GaSb with higher ratios of Sb monomers-to-dimers was considered. By increasing the Sb source's cracking zone temperature, a greater number of Sb tetramers and dimers are cracked into monomers. Previous reports of GaSb grown with more monomers have shown improvements in material quality, thought to be due to Sb monomers acting as trap getters. To test the validity of this, photoluminescence and dark current measurements were used. First, two GaSb photocapacitance samples were grown, both at T2SL growth temperature, one with the Sb cracker at 900°C and the other at 1100°C. Then, two 8/8 T2SL samples were grown, with the same Sb cracker temperatures as above. All of the samples with higher Sb cracker temperatures showed a four-fold reduction of surface defects visible with Nomarski microscopy. Photoluminescence intensity also improved; with the Sb cracker at 1100°C, the intensity was twice as high as the sample grown with the cracker at 900°C. However, the recipe for higher cracker temperatures did not perform as well for dark current levels. Two 10/10 T2SL samples with n-i-p architecture were

grown and fabricated, and dark currents were found to be 1-2 orders of magnitude higher in the sample grown with the Sb cracker at 1100°C, compared to the 900°C sample. The higher dark current levels in the samples grown with increased Sb cracker temperatures are most likely due to impurities from the growth chamber.

There are several avenues for future work for this experiment. Higher-temperature bake-out sessions for the Sb cracker, trying a broader range of cracking zone and substrate temperatures, or growing in a different MBE are a few examples. There may be other ways to improve the GaSb during growth as well. Svensson [40] suggested exposing a sample to hydrogen during growth as a way to mitigate defects. A combination of photocapacitance, dark current, and TRPL characterizations could be used to show potential improvements in lifetime, pinpoint defect energy levels, and correlate device performance with growth methods.

The photocapacitance measurements could, in general, be improved by going to lower temperatures. Previously in this chapter, the effect of sample temperature on photocapacitance measurements was shown. It was clear that as the sample temperature was lowered, more changes in the photocapacitance plots became visible. This would be especially important for T2SL characterization, which has a much narrower bandgap than the GaSb.

Appendix A

Lifetime Measurement Techniques

A.1 Carrier lifetime measurement techniques

This section outlines several key lifetime measurement techniques for T2SL reported in literature, that were not covered in Chapter 4.

A.1.1 Photoconductive response

Photoconductive response (PCR) is an indirect, no-assumption measurement of carrier lifetime (τ), described and used by Yang [36]. The lifetime is extracted by measuring mobility (μ_e, μ_h) and change in conductivity ($\Delta\sigma_{xx}$) as a function of incident light (I). These are related to lifetime by:

$$\frac{\Delta\sigma_{xx}}{\sigma^0_{xx}} = \frac{\Delta ne(\mu_e + \mu_h)}{n_0 e\mu_e + p_0 e\mu_h} = \frac{(1-R)I\alpha\tau(\mu_e + \mu_h)}{\hbar\omega(n_0\mu_e + p_0\mu_h)} \tag{A.1}$$

where σ^0_{xx} is the conductivity without illumination, n,n_0, p_0 are the carrier densities of photogenerated electrons, electrons without illumination, and holes without illumination, respectively, R is the reflection coefficient, α is the absorption coefficient,

and $\hbar$ is Planck's constant. Since I is known and α, R, mobilities, and conductivities are measured, τ can be determined by a linear fit of $\frac{\Delta\sigma_{xx}}{\sigma^0_{xx}}$ as a function of I.

A.1.2 Electron-beam-induced current

Electron-beam-induced current (EBIC) uses an electron beam to excite electron-hole pairs to measure the diffusion length and lifetime of minority carriers. The generic theory and method is discussed by [80], while measurements on T2SL is presented in Li 2004 and Zuo 2013 [37, 45]. A device used in an EBIC measurement will can be either a p-n junction or a Schottky diode. Mesas are etched on the sample, contact metals are deposited, and diodes are cleaved through the center of the mesa to expose a cross-section of the p-n junction. These samples are loaded into a scanning electron microscope (SEM) and electrically connected to a current meter (ammeter). An electron beam incident on the sample causes a current to form, which is measured as a function of electron beam position. The measured current (I) is related to the diffusion length (L) and electron beam position (d) by $I(d) \propto (e^{-d/L})/d^{3/2}$ [80]. Zuo [45] used a model which assumed values for vertical mobility and the surface recombination-to-diffusion ratio to fit the data to extract carrier lifetimes. Li [37] reported a similar approach, where a model simulating the EBICurrent was fitted to the data to extract diffusion length. To get carrier lifetime, this measured diffusion length and an assumed mobility (μ) were used:

$$\tau = L^2/D = L^2/(\mu kT/q) \tag{A.2}$$

where k is Boltzmann's constant, T is sample temperature, and q is electronic charge. Because assumptions have to be made about the vertical mobility in this method, the accuracy of the absolute lifetime must be questioned. Even samples in the same study may have different vertical mobilities, making even comparisons of samples within the

same study tenuous.

A.1.3 Current-voltage data fitting

Minority carrier lifetimes have also been obtained by fitting to I-V data from pn-junction devices [38, 81]. This is performed using equations for current modeling, including generation-recombination (J_{G-R}), diffusion (J_{diff}), direct tunneling (J_T), and trap-assisted tunneling (J_{TAT}) current densities. Of these current densities, J_{diff} contains carrier lifetime components. The diffusion current density is written as:

$$J_{diff} = n_i^2 \sqrt{qkT} \left(\frac{1}{N_A} \sqrt{\mu_e/\tau_e} + \frac{1}{N_D} \sqrt{\mu_h/\tau_h} \right) (e^{qV/kT} - 1) \tag{A.3}$$

and depends on the intrinsic carrier concentration (n_i), the acceptor (N_A) and donor (N_D) doping concentrations and the electron (τ_e) and hole (τ_h) lifetimes. Fitting all the current components and using assumptions about carrier mobilities, effective mass, and trap density, carrier lifetimes can be extracted from current-voltage data.

A.1.4 Optical Modulation Response

Optical modulation response (OMR) is a frequency-domain method that measures the intensity of PL as a function of incident laser modulation frequency and intensity to determine carrier lifetime [39, 82, 42, 40, 43]. The sample architecture in this measurement is designed to minimize the effects of surface recombination, with aluminum-based layers (typically AlSb or AlGaSb) sandwiching the material of interest, that segregate the bulk material from the surface. A laser with tunable modulation frequency (ω) is incident on the sample. The sample absorbs the light, promoting electrons to the conduction band. After some time, the electrons return to the valence band, emitting a photon in the process known as photoluminescence. This light is collected and focused onto a broad-band detector whose output is connected

to a lock-in amplifier to measure PL intensity as a function of modulation frequency. Knowing the modulated carrier generation rate (G_1), the lifetime is found by fitting

$$I_{PL}(\omega) \propto \frac{G_1\tau}{\sqrt{1+\omega^2\tau^2}} \tag{A.4}$$

to the data. Collecting the lifetime for a number of excitation levels makes a lifetime vs. excitation intensity plot; using linear extrapolation, the lifetime for zero excitation power can be obtained. Because OMR does not rely on assumptions, it is a good though indirect method for determining carrier lifetime.

A.1.5 Time-Resolved Differential Transmission

Time-resolved differential transmission (TRDT) is a pump-probe measurement that monitors transient changes in sample transmission, used to determine ultrafast carrier dynamics such as carrier lifetime[44, 83]. Like OMR, samples for TRDT use cladding layers surrounding the material of interest to reduce the effects surface recombination. Two pulsed lasers, a pump laser with higher energy (lower wavelength) and a probe with lower energy (higher wavelength), are used for this measurement. The two laser spots are spatially overlapped on the sample but delayed in time. The pump pulse arrives first, creating excess minority carriers and then the probe beam arrives after a specific time delay. The transmission of the probe is measured as a function of its time delay, which provides recombination rates. Collecting the differential transmission for a number of excess carrier densities enables a measurement of the carrier lifetime, with a fit to the carrier-dependent recombination rate equation:

$$R(N) = A + BN + CN^2 \tag{A.5}$$

where R is the recombination rate (s^{-1}), N is the excess carrier density (cm^{-3}), and A, B, and C are the SRH, radiative, and Auger recombination coefficients, respectively.

For the case of T2SL under low-injection conditions where only SRH is present and is independent of excess carrier density, the radiative and Auger terms can be neglected; for materials where these coefficients cannot be ignored, the sample's coefficients have to be measured, calculated, or assumed in order to perform the fit. For T2SL, TRDT is a direct measure of carrier lifetime with no assumptions, providing highly reliable lifetime figures.

References

[1] E. R. Youngdale, J. R. Meyer, C. A. Hoffman, F. J. Bartoli, C. H. Grein, P. M. Young, H. Ehrenreich, R. H. Miles, and D. H. Chow. Auger lifetime enhancement in InAs-$Ga_{1-x}In_xSb$ superlattices. *Applied Physics Letters*, 64(23):3160, 1994.

[2] A Rogalski. History of infrared detectors. *Opto-Electronics Review*, 20(3):279–308, 2012.

[3] S.D. Gunapala. Semiconductors and Semimetals (84) Advances in Infrared Photodetectors. In Sarath D. Gunapala, David R Rhiger, and Chennupati Jagadish, editors, *Advances in Infrared Photodetectors*, volume 84, pages vii–viii. Elsevier, 2011.

[4] A. Rogalski, K. Adamiec, and J. Rutkowski. *Narrow-Gap Semiconductor Photodiodes*. SPIE Press, 2000.

[5] Zhores Alferov. Double Heterostructure Lasers : Early Days and Future Perspectives. *IEEE Journal on selected topics in quantum electronics*, 6(6):832–840, 2000.

[6] H. Kroemer. A Proposed Class of Heterojunction Injection Lasers. *Proceedings of the IEEE*, 51:1782–1783, 1963.

[7] S.M. Sze. *Physics of Semiconductor Devices*. John Wiley & Sons, New York, 1981.

[8] S.O. Kasap. *Optoelectronics and Photonics: Principles and Practices*. Prentice Hall, 2001.

[9] L. Esaki and R. Tsu. Superlattice and Negative Differential Conductivity in Semiconductors. *IBM J. Res. Develop.*, 14(1):61–65, 1970.

[10] G. A. Sai-Halasz, R. Tsu, and L. Esaki. A new semiconductor superlattice. *Applied Physics Letters*, 30(12):651, 1977.

[11] David Z-Y. Ting, Alexander Soibel, Linda Höglund, Jean Nguyen, Cory J Hill, Arezou Khoshakhlagh, and Sarath D Gunapala. Chapter 1 - Type-II Superlattice Infrared Detectors. In Sarath D. Gunapala, David R Rhiger, and Chennupati Jagadish, editors, *Advances in Infrared Photodetectors*, volume 84, pages 1–57. Elsevier, 2011.

[12] D.L. Smith and C. Mailhiot. Proposal for strained type II superlattice infrared detectors. *Journal of Applied Physics*, 62(6):2545–2548, 1987.

[13] X. B. Zhang, J. H. Ryou, R. D. Dupuis, A. Petschke, S. Mou, S. L. Chuang, C. Xu, and K. C. Hsieh. Metalorganic chemical vapor deposition growth of high-quality InAs/GaSb type II superlattices on (001) GaAs substrates. *Applied Physics Letters*, 88(7):072104, 2006.

[14] Y. Huang, J.-H. Ryou, R.D. Dupuis, V.R. D'Costa, E.H. Steenbergen, J. Fan, Y.-H. Zhang, a. Petschke, M. Mandl, and S.-L. Chuang. Epitaxial growth and characterization of InAs/GaSb and InAs/InAsSb type-II superlattices on GaSb substrates by metalorganic chemical vapor deposition for long wavelength infrared photodetectors. *Journal of Crystal Growth*, 314(1):92–96, January 2011.

[15] Robert Rehm, Martin Walther, Johannes Schmitz, Matthias Wauro, Wolfgang Luppold, Jasmin Niemasz, Frank Rutz, Andreas Wörl, Jan-Michael Masur, Lutz

Kirste, Ralf Scheibner, Joachim Wendler, and Johann Ziegler. Substrate removal of dual-colour InAs/GaSb superlattice focal plane arrays. *Physica Status Solidi (C)*, 9(2):318–321, February 2012.

[16] M. Razeghi, A. Haddadi, A.M. Hoang, E.K. Huang, G. Chen, S. Bogdanov, S.R. Darvish, F. Callewaert, and R. McClintock. Advances in antimonide-based Type-II superlattices for infrared detection and imaging at center for quantum devices. *Infrared Physics & Technology*, 59:41–52, July 2013.

[17] W.E. Tennant, Donald Lee, Majid Zandian, Eric Piquette, and Michael Carmody. MBE HgCdTe Technology: A Very General Solution to IR Detection, Described by Rule 07, A Very Convenient Heuristic. *Journal of Electronic Materials*, 37(9):1406–1410, March 2008.

[18] W. E. Tennant. Rule 07 Revisited: Still a Good Heuristic Predictor of p/n HgCdTe Photodiode Performance? *Journal of Electronic Materials*, 39(7):1030–1035, February 2010.

[19] Herbert Kroemer. The 6.1 Å family (InAs, GaSb, AlSb) and its heterostructures: a selective review. *Physica E: Low-dimensional Systems and Nanostructures*, 20:196–203, January 2004.

[20] H. S. Kim, E. Plis, J. B. Rodriguez, G. D. Bishop, Y. D. Sharma, L. R. Dawson, S. Krishna, J. Bundas, R. Cook, D. Burrows, R. Dennis, K. Patnaude, A. Reisinger, and M. Sundaram. Mid-IR focal plane array based on type-II InAs/GaSb strain layer superlattice detector with nBn design. *Applied Physics Letters*, 92(18):183502, 2008.

[21] David Z.-Y. Ting, Cory J. Hill, Alexander Soibel, Sam A. Keo, Jason M. Mumolo, Jean Nguyen, and Sarath D. Gunapala. A high-performance long wavelength

superlattice complementary barrier infrared detector. *Applied Physics Letters*, 95(2):023508, 2009.

[22] Binh-Minh Nguyen, Darin Hoffman, Pierre-Yves Delaunay, and Manijeh Razeghi. Dark current suppression in type II InAs/GaSb superlattice long wavelength infrared photodiodes with M-structure barrier. *Applied Physics Letters*, 91(16):163511, 2007.

[23] Nutan Gautam, Stephen Myers, Ajit V. Barve, Brianna Klein, E.P. Smith, Dave Rhiger, Elena Plis, Maya N. Kutty, Nathan Henry, Ted Schuler-Sandy, and S. Krishna. Band engineered HOT midwave infrared detectors based on type-II InAs/GaSb strained layer superlattices. *Infrared Physics & Technology*, 59:72–77, July 2013.

[24] Z.-B. Tian, T. Schuler-Sandy, and S. Krishna. Electron barrier study of mid-wave infrared interband cascade photodetectors. *Applied Physics Letters*, 103(8):083501, 2013.

[25] Sumith Bandara, Patrick Maloney, Neil Baril, Joseph Pellegrino, and Meimei Tidrow. Performance of InAs/GaSb superlattice infrared detectors and dependence on minority carrier lifetime. *Infrared Physics & Technology*, 54(3):263–266, May 2011.

[26] C. H. Grein, H. Cruz, M. E. Flatte, and H. Ehrenreich. Theoretical performance of very long wavelength InAs/$In_xGa_{1-x}Sb$ superlattice based infrared detectors. *Applied Physics Letters*, 65(20):2530, 1994.

[27] David R. Rhiger. Performance Comparison of Long-Wavelength Infrared Type II Superlattice Devices with HgCdTe. *Journal of Electronic Materials*, 40(8):1815–1822, May 2011.

[28] G. A. Umana-Membreno, B. Klein, H. Kala, J. Antoszewski, N. Gautam, M. N. Kutty, E. Plis, S. Krishna, and L. Faraone. Vertical minority carrier electron transport in p-type InAs/GaSb type-II superlattices. *Applied Physics Letters*, 101(25):253515, 2012.

[29] Koushik Banerjee, Siddhartha Ghosh, Elena Plis, and Sanjay Krishna. Study of Short- and Long-Term Effectiveness of Ammonium Sulfide as Surface Passivation for InAs/GaSb Superlattices Using X-Ray Photoelectron Spectroscopy. *Journal of Electronic Materials*, 39(10):2210–2214, June 2010.

[30] Blair C. Connelly, Grace D. Metcalfe, Hongen Shen, and Michael Wraback. Study of recombination mechanisms limiting the performance of Sb-based III-V type II superlattices for infrared detectors. In Paul D. LeVan, Ashok K. Sood, Priyalal S. Wijewarnasuriya, Manijeh Razeghi, Jose Luis Pau Vizcaíno, Rengarajan Sudharsanan, Melville P. Ulmer, and Tariq Manzur, editors, *Proc. SPIE*, volume 8155, page 81550L, September 2011.

[31] L. A. Coldren and S. W. Corzine. *Diode Lasers and Photonic Integrated Circuits*. John Wiley & Sons, Inc, 1995.

[32] Richard K. Ahrenkiel. Chapter 2: Minority-Carrier Lifetime in III-V Semiconductors. In Richard K. Ahrenkiel and Mark S. Lundstrom, editors, *Minority Carriers In III-V Semiconductors: Physics and Applications, Semiconductors and Semimetals*, volume 39, pages 39–150. Elsevier, 1993.

[33] J.I. Pankove. *Optical Processes in Semiconductors*. Dover, New Jersey, 1971.

[34] J.M. Liu. *Photonic Devices*. Cambridge University Press, United Kingdom, 2005.

[35] E. R. Youngdale. Recombination lifetime in $InAsGa_{1-x}In_xSb$ superlattices. *Journal of Vacuum Science & Technology B: Microelectronics and Nanometer Structures*, 12(2):1129, March 1994.

[36] Q. K. Yang, C. Pfahler, J. Schmitz, W. Pletschen, and F. Fuchs. Trap centers and minority carrier lifetimes in InAs /(GaIn)Sb superlattice long wavelength photodetectors. In Manijeh Razeghi and Gail Brown, editors, *Proc. SPIE*, volume 4999, pages 448–456, 2003.

[37] Jian V. Li, Shun Lien Chuang, Eric M. Jackson, and Edward Aifer. Minority carrier diffusion length and lifetime for electrons in a type-II InAs/GaSb superlattice photodiode. *Applied Physics Letters*, 85(11):1984–1986, 2004.

[38] J. Pellegrino and R. DeWames. Minority carrier lifetime characteristics in type II InAs/GaSb LWIR superlattice $n^+\pi p^+$. In B.F Andresen, G.F. Fulop, and P.R. Norton, editors, *Proc. SPIE*, volume 7298, page 72981U. Spie, 2009.

[39] Dmitry Donetsky, Stefan P. Svensson, Leonid E. Vorobjev, and Gregory Belenky. Carrier lifetime measurements in short-period InAs/GaSb strained-layer superlattice structures. *Applied Physics Letters*, 95(21):212104, 2009.

[40] S.P. Svensson, D. Donetsky, D. Wang, H. Hier, F.J. Crowne, and G. Belenky. Growth of type II strained layer superlattice, bulk InAs and GaSb materials for minority lifetime characterization. *Journal of Crystal Growth*, 334(1):103–107, November 2011.

[41] Blair C. Connelly, Grace D. Metcalfe, Hongen Shen, and Michael Wraback. Direct minority carrier lifetime measurements and recombination mechanisms in long-wave infrared type II superlattices using time-resolved photoluminescence. *Applied Physics Letters*, 97(25):251117, 2010.

[42] Dmitry Donetsky, Gregory Belenky, Stefan Svensson, and Sergei Suchalkin. Minority carrier lifetime in type-2 InAs-GaSb strained-layer superlattices and bulk HgCdTe materials. *Applied Physics Letters*, 97(5):052108, 2010.

[43] Sumith Bandara, Patrick Maloney, Neil Baril, Joseph Pellegrino, and Meimei Tidrow. Doping dependence of minority carrier lifetime in long-wave Sb-based type II superlattice infrared detector materials. *Optical Engineering*, 50(6):061015–1, 2011.

[44] B. V. Olson, E. A. Shaner, J. K. Kim, J. F. Klem, S. D. Hawkins, L. M. Murray, J. P. Prineas, M. E. Flatte, and T. F. Boggess. Time-resolved optical measurements of minority carrier recombination in a mid-wave infrared InAsSb alloy and InAs/InAsSb superlattice. *Applied Physics Letters*, 101(9):092109, 2012.

[45] Daniel Zuo, Pengfei Qiao, Daniel Wasserman, and Shun Lien Chuang. Direct observation of minority carrier lifetime improvement in InAs/GaSb type-II superlattice photodiodes via interfacial layer control. *Applied Physics Letters*, 102(14):141107, 2013.

[46] L. M. Murray, K. S. Lokovic, B. V. Olson, A. Yildirim, T. F. Boggess, and J. P. Prineas. Effects of growth rate variations on carrier lifetime and interface structure in InAs/GaSb superlattices. *Journal of Crystal Growth*, 386(0):194–198, January 2014.

[47] E. H. Steenbergen, B. C. Connelly, G. D. Metcalfe, H. Shen, M. Wraback, D. Lubyshev, Y. Qiu, J. M. Fastenau, A. W. K. Liu, S. Elhamri, O. O. Cellek, and Y.-H. Zhang. Significantly improved minority carrier lifetime observed in a long-wavelength infrared III-V type-II superlattice comprised of InAs/InAsSb. *Applied Physics Letters*, 99(25):251110, 2011.

[48] Blair C. Connelly, Grace D. Metcalfe, Hongen Shen, Michael Wraback, Chadwick L. Canedy, Igor Vurgaftman, Joseph S. Melinger, Chaffra A. Affouda, Eric M. Jackson, Jill A. Nolde, Jerry R. Meyer, and Edward H. Aifer. Investigation of Trap States in Mid-Wavelength Infrared Type II Superlattices

Using Time-Resolved Photoluminescence. *Journal of Electronic Materials*, 42(11):3203–3210, September 2013.

[49] D.K. Schroder. *Semiconductor Material and Device Characterization*. Wiley-Interscience, New York, 3 edition, 2006.

[50] H. Bracht, S.P. Nicols, W. Walukiewicz, J.P. Silveira, F. Briones, and E.E. Haller. Large disparity between gallium and antimony self-diffusion in gallium antimonide. *Nature*, 408(6808):69–72, 2000.

[51] H. Bracht, S. P. Nicols, E. E. Haller, J. P. Silveira, and F. Briones. Self-diffusion in $^{69}Ga^{121}Sb/^{71}Ga^{123}Sb$ isotope heterostructures. *Journal of Applied Physics*, 89(10):5393–5399, 2001.

[52] K. Y. Cheng. Development of molecular beam epitaxy technology for IIIV compound semiconductor heterostructure devices. *Journal of Vacuum Science & Technology A: Vacuum, Surfaces, and Films*, 31(5):050814, 2013.

[53] A.S. Bracker, M.J. Yang, B.R. Bennett, J.C. Culbertson, and W.J. Moore. Surface reconstruction phase diagrams for InAs, AlSb, and GaSb. *Journal of Crystal Growth*, 220:384–392, December 2000.

[54] M. Yano, M. Nogami, Y. Matsushima, and M. Kimata. Molecular Beam Epitaxial Growth of InAs. *Japanese Journal of Applied Physics*, 16(12):2131–2137, 1977.

[55] V. Sallet, L. Largeau, O. Mauguin, L. Travers, and J. C. Harmand. MBE growth of InAsN on (100) InAs substrates. *Physica Status Solidi (B)*, 242(6):R43–R45, May 2005.

[56] Silvia Butera, Richard T. Moug, Peter Vines, Gerald S. Buller, and Kevin A. Prior. Direct growth of ZnSe and CdSe on (100) InAs substrates. *Physica Status Solidi (C)*, 3:n/a–n/a, March 2014.

[57] E.H.C. Parker, editor. *The Technology and physics of molecular beam epitaxy.* Plenum Press, New York, 1985.

[58] E. Plis, A. Khoshakhlagh, S. Myers, H. S. Kim, N. Gautam, Y. D. Sharma, S. Krishna, S. J. Lee, and S. K. Noh. Molecular beam epitaxy growth and characterization of type-II InAs/GaSb strained layer superlattices for long-wave infrared detection. *Journal of Vacuum Science & Technology B: Microelectronics and Nanometer Structures*, 28(3):C3G13, 2010.

[59] E. Plis, H. S. Kim, G. Bishop, S. Krishna, K. Banerjee, and S. Ghosh. Lateral diffusion of minority carriers in nBn based type-II InAs/GaSb strained layer superlattice detectors. *Applied Physics Letters*, 93(12):123507, 2008.

[60] N. Gautam. *Unipolar Barrier Strained Layer Superlattice Infrared Photodiodes: Physics and Barrier Engineering.* PhD thesis, University of New Mexico, 2012.

[61] R. K. Ahrenkiel, B. M. Keyes, and D. J. Dunlavy. Intensity-dependent minority-carrier lifetime in III-V semiconductors due to saturation of recombination centers. *Journal of Applied Physics*, 70(1):225, 1991.

[62] Brianna Klein, Nutan Gautam, Elena Plis, Ted Schuler-sandy, Thomas J Rotter, Sanjay Krishna, C Blair, Grace D Metcalfe, Paul Shen, and Michael Wraback. Carrier lifetime studies in midwave infrared type-II InAs / GaSb strained layer superlattice. *Journal of Vacuum Science & Technology B*, 32(2):02C101, 2014.

[63] Brian R. Bennett, B. V. Shanabrook, R. J. Wagner, John L. Davis, and J. R. Waterman. Control of interface stoichiometry in InAs/GaSb superlattices grown by molecular beam epitaxy. *Applied Physics Letters*, 63(7):949, 1993.

[64] Brian R. Bennett, B. V. Shanabrook, and M. E. Twigg. Anion control in molecular beam epitaxy of mixed As/Sb III-V heterostructures. *Journal of Applied Physics*, 85(4):2157, 1999.

[65] Qianghua Xie, J. E. Van Nostrand, J. L. Brown, and C. E. Stutz. Arsenic for antimony exchange on GaSb, its impacts on surface morphology, and interface structure. *Journal of Applied Physics*, 86(1):329, 1999.

[66] M. E. Twigg, B. R. Bennett, B. V. Shanabrook, J. R. Waterman, J. L. Davis, and R. J. Wagner. Interfacial roughness in InAs/GaSb superlattices. *Applied Physics Letters*, 64(25):3476, 1994.

[67] J. T. Zborowski, A. Vigliante, S. C. Moss, and T. D. Golding. Interface properties of (In,Ga)Sb/InAs heterostructures. *Journal of Applied Physics*, 79(11):8379, 1996.

[68] J. Steinshnider, J. Harper, M. Weimer, C.H. Lin, S.S. Pei, and D.H. Chow. Origin of antimony segregation in GaInSb/InAs strained-layer superlattices. *Physical review letters*, 85(21):4562–5, November 2000.

[69] D. V. Lang. Deep-level transient spectroscopy: A new method to characterize traps in semiconductors. *Journal of Applied Physics*, 45(7):3023, 1974.

[70] S. Dhar, Kanad Mallik, and Mousumi Mazumdar. Electron traps in GaAs:Sb grown by liquid phase epitaxy. *Journal of Applied Physics*, 77(4):1531, 1995.

[71] S. Dhar and M. Mazumdar. Hall and photocapacitance analyses of the Sb-related electron trap in 0 . 02) layers grown. *Semicond. Sci. Technol.*, 15:622–624, 2000.

[72] Kanad Mallik, Sunanda Dhar, and S. Sinha. A photoluminescence and photocapacitance study of GaAs : In and GaAs : Sb layers grown by liquid-phase epitaxy. *Semiconductor Science and Technology*, 9:1649–1653, 1994.

[73] D Neamen. *Semiconductor Physics and Devices*. McGraw-Hill, 2003.

[74] P. S. Dutta, H. L. Bhat, and Vikram Kumar. The physics and technology of gallium antimonide: An emerging optoelectronic material. *Journal of Applied Physics*, 81(9):5821, 1997.

[75] B.L. Sharma, editor. *Metal-Semiconductor Schottky Barrier Junctions and Their Applications*. Plenum Press, New York, 1984.

[76] Meng-Chyi Wu and Chi-Ching Chen. Photoluminescence of high-quality GaSb grown from Ga- and Sb-rich solutions by liquid-phase epitaxy. *Journal of Applied Physics*, 72(9):4275, 1992.

[77] Eiichi Kuramochi, Naoto Kondo, Yoshifumi Takanashi, and Masatomo Fujimoto. Observation of deep levels in undoped GaSb grown by molecular beam epitaxy. *Applied Physics Letters*, 63(19):2664, 1993.

[78] Qianghua Xie, J E Van Nostrand, R L Jones, J Sizelove, and D C Look. Electrical and optical properties of undoped GaSb grown by molecular beam epitaxy using cracked Sb1 and Sb2. *Journal of Crystal Growth*, 207:255–265, 1999.

[79] P. D. Brewer, D.H. Chow, and R.H. Miles. Atomic antimony for molecular beam epitaxy of high quality IIIV semiconductor alloys. *Journal of Vacuum Science & Technology B*, 14(3):2335–2338, May 1996.

[80] D.E. Ioannou. A SEM-EBIC minority-carrier lifetime-measurement technique. *J. Phys. D.*, 13:611–616, 1980.

[81] Q. K. Yang, F. Fuchs, J. Schmitz, and W. Pletschen. Investigation of trap-assisted tunneling current in InAs/(GaIn)Sb superlattice long-wavelength photodiodes. *Applied Physics Letters*, 81(25):4757, 2002.

[82] D. Donetsky, S. Anikeev, N. Gu, G. Belenky, S. Luryi, C.A. Wang, D.A. Shiau, M. Dashiell, J. Beausang, and G. Nichols. Analysis of Recombination Processes

in 0.50.6 eV Epitaxial GaInAsSb Lattice-matched to GaSb. *AIP Conference Proceedings*, 738(2004):320–328, 2004.

[83] Rohit P. Prasankumar, Prashanth C. Upadhya, and Antoinette J. Taylor. Ultrafast carrier dynamics in semiconductor nanowires. *Physica Status Solidi (B)*, 246(9):1973–1995, September 2009.